PPPL-2575

UC-427

PPPL-2575

NUMERICAL SOLUTIONS OF MAGNETOHYDRODYNAMIC STABILITY OF AXISYMMETRIC TOROIDAL PLASMAS USING CUBIC B-SPLINE FINITE ELEMENT METHOD

By

C.Z. Cheng

DECEMBER 1988

PLASMA
PHYSICS
LABORATORY

NOTICE

Printed in the United States of America

Available from:

National Technical Information Service
U.S. Department of Commerce
5285 Port Royal Road
Springfield, Virginia 22161

Price Printed Copy $ * ; Microfiche $4.50

*Pages	NTIS Selling Price
1-25	$7.00
25-50	$8.50
51-75	$10.00
76-100	$11.50
101-125	$13.00
126-150	$14.50
151-175	$16.00
176-200	$17.50
201-225	$19.00
226-250	$20.50
251-275	$22.00
276-300	$23.50
301-325	$25.00
326-350	$26.50
351-375	$28.00
376-400	$29.50
401-425	$31.00
426-450	$32.50
451-475	$34.00
476-500	$35.50
500-525	$37.00
526-550	$38.50
551-575	$40.00
567-600	$41.50

For documents over 600 pages, add $1.50 for each additional 25-page increment.

NUMERICAL SOLUTIONS OF MAGNETOHYDRODYNAMIC STABILITY OF AXISYMMETRIC TOROIDAL PLASMAS USING CUBIC B-SPLINE FINITE ELEMENT METHOD *

C. Z. Cheng

Princeton Plasma Physics Laboratory

P.O. Box 451, Princeton, NJ 08543 USA

PPPL--2575

DE89 004635

Abstract

A nonvariational ideal MHD stability code (NOVA) has been developed. In a general flux coordinate (ψ,θ,ζ) system with an arbitrary Jacobian, the NOVA code employs Fourier expansions in the generalized poloidal angle θ and generalized toroidal angle ζ directions, and cubic-B spline finite elements in the radial ψ direction. Extensive comparisons with these variational ideal MHD codes show that the NOVA code converges faster and gives more accurate results. An extended version of NOVA is developed to integrate non-Hermitian eigenmode equations due to energetic particles. The set of non-Hermitian integro-differential eigenmode equations is numerically solved by the NOVA-K code. We have studied the problems of the stabilization of ideal MHD internal kink modes by hot particle pressure and the excitation of "fishbone" internal kink modes by resonating with the energetic particle magnetic drift frequency. Comparisons with analytical solutions show that the values of the critical β_h from the analytical theory can be an order of magnitude different from those computed by the NOVA-K code.

*Presented as Invited Talk, 7th Intl. Conf. on Finite Element Methods in Flow Problems, Univ. of Alabama, Huntsville, ALA, April 3-7, 1989.

I. Introduction

Linear stability analysis of magnetohydrodynamic (MHD) modes in axisymmetric toroidal plasmas is crucial to thermonuclear fusion research. In particular, ideal MHD instabilities are thought to play an important role in limiting the β-values of tokamak plasmas and causing tokamak disruptions. The mathematical problem is to solve the two-dimensional eigenmode equations and obtain the growth rates of the MHD instabilities. Exact solutions are impossible to obtain without the use of numerical computations. A number of two-dimensional normal mode codes [1-7] have been developed extensively to study the dependence of ideal MHD instabilities on a variety of parameters relating to the geometry as well as the pressure and current profiles. As practical tools, they are used to aid in the design of new experiments and in the analysis of experimental data. Most of these ideal MHD codes [1-6] utilize a Lagrangian formalism [8] for linearized perturbations and involve the use of the linear Galerkin procedure, which reduces the problem to the minimization of an algebraic quadratic form with respect to a certain set of variational parameters. The variational calculation is then reduced to the determination of eigenvalues and eigenfunctions of the matrix eigenvalue problem.

Nonetheless, the inherent limitation of these variational codes is that because of their variational nature, they cannot be extended to the stability calculations of the non-Hermitian eigenmode equations, such as in the cases of ideal MHD with equilibrium flows, resistive MHD and kinetic MHD, etc., where variational energy principles cannot be established. In particular, present-day tokamak experiments and future fusion reactors will involve energetic particles that will have significant effects on the MHD modes. In the high-power, nearly perpendicular neutral beam injection experiments, bursts of

large amplitude m=n=1 MHD fluctuations, dubbed "fishbones" were observed in the Mirnov coil and x-ray signals [9]. These fishbone bursts are found to be correlated with the reductions of neutron emissivity which represent significant losses of energetic beam ions, and thus play an important role in limiting the β-values of tokamak devices. In future tokamak reactors, α-particles may destabilize the toroidicity induced shear Alfvén modes [10,11] and their consequences are yet to be determined. For the low frequency MHD waves, the energetic particle dynamics are not governed by MHD fluid equations because $\omega < \omega_d$, where ω_d is the magnetic drift frequency. Instead their dynamics are governed by gyrokinetic equations and the resultant eigenmode equations are non-Hermitian integro-differential equations.

In this paper, we present a nonvariational MHD stability code (NOVA). The ideal MHD version of the NOVA code has previously been published [7]. All these variational ideal MHD stability codes [1-6] employ linear finite elements in the minor radius direction, which are the lowest order finite elements allowed for representing the displacement vector ξ. Since they are in quadratic form, the numerical errors in the eigenvalues, ω, scale as N^{-2}, where N is the total number of the radial computational grid points. Therefore, our nonvariational approach requires higher order finite elements to achieve better accuracy and faster convergence. For example, with cubic B-spline finite elements [12-15] the errors in ω scale as N^{-4}. In general a flux coordinate (ψ,θ,ζ) system with an arbitrary Jacobian, the NOVA code employs Fourier expansion in the poloidal angle θ direction, as in the PEST code, and cubic B-spline finite elements in the radial ψ direction. An arbitrary nonuniform ψ-mesh is set up to provide the option of zoning the mesh to allow more finite elements near rational surfaces, the plasma edge, and the magnetic axis. In comparison with these existing variational ideal MHD

stability codes [1-6], the NOVA code converges faster and gives more accurate results.

In the following, we first briefly describe in Sec. II the anisotropic MHD equilibrium and present a class of generalized toroidal coordinate systems which can greatly improve the representation of various MHD instabilities. In Sec. III, we formulate the kinetic MHD eigenmode equations and the corresponding boundary conditions for our nonvariational treatment. The numerical methods which involve cubic-B spline finite elements, are described in Sec. IV. Convergence studies of the ideal MHD version of the NOVA code are presented for the analytical Solovev equilibria [16], and detailed comparisons, as presented with other variational codes [17], are given in Sec. V. In Sec. VI we study the effects of neutral beam injections on the internal kink mode and the excitation of fishbone modes. We establish the correctness of the NOVA-K code (kinetic version of NOVA) by both convergence studies and qualitative agreements with numerical solutions of a simplified analytical dispersion [18]. However, comparisons with analytical results show that the critical values of the energetic particle beta for the stabilization of the ideal MHD internal kink and the destabilization of the resonant fishbone mode can be an order of magnitude different from those computed by the NOVA-K code. In addition, a necessary condition for the excitation of fishbone mode, $\beta > \beta_{crit}$, is found, where β is the total plasma beta and β_{crit} is the critical beta for the ideal MHD internal kink instability. This is contrary to the analytical results that show that $\beta_{crit} = 0$. In Sec. VII, we summarize the principal conclusions of this work.

II. Anisotropic Toroidal MHD Equilibrium and Flux Coordinate System

We consider stationary anisotropic ideal MHD equilibria satisfying

$$\vec{J} \times \vec{B} = \nabla\cdot\vec{P} = \nabla P_\perp + \nabla\cdot\left[(P_\parallel - P_\perp)\hat{e}_B\hat{e}_B\right] \quad ,$$

$$\nabla \times \vec{B} = \vec{J}, \quad \text{and} \quad \nabla\cdot\vec{B} = 0 \quad , \tag{1}$$

where $\hat{e}_B = \vec{B}/B$, and $\vec{J}$, $\vec{B}$ and $\vec{P}$ are the equilibrium current, magnetic field, and pressure tensor, respectively. $\vec{P}$ is obtained by specifying the particle guiding center distribution for each species $F(\varepsilon,\mu,\psi_g)$ where energy $\varepsilon = v^2/2$ and magnetic moment $\mu = v_\perp^2/2B$ are the constants of motions, and ψ_g is the magnetic flux position of the guiding center. The parallel and perpendicular pressures are given by

$$\begin{pmatrix} P_\parallel \\ P_\perp \end{pmatrix} = \sum_{j,\sigma} 2\pi m_j \int \frac{d\varepsilon d\mu B}{|v_{\parallel j}|} F_j \begin{pmatrix} 2\varepsilon - \mu B \\ \mu B \end{pmatrix} . \tag{2}$$

From Eq. (1), we obtain the perpendicular momentum balance equation

$$\nabla_\perp(B^2/2 + P_\perp) = \vec{\kappa}\left[B^2 + (P_\perp - P_\parallel)\right] \quad , \tag{3}$$

and the parallel momentum balance equation

$$\vec{B}\cdot\nabla P_\parallel = (P_\parallel - P_\perp)\hat{e}_B\cdot\nabla B \quad , \tag{4}$$

where $\vec{\kappa} = \hat{e}_B\cdot\nabla\hat{e}_B$ is the curvature. Note that Eq. (4) is automatically satisfied if $F(\varepsilon,\mu,\psi_g)$ is used.

In terms of the flux coordinate system (ψ,θ,ζ), the equilibrium with nested magnetic surface can be written as

$$\vec{B} = \nabla\zeta \times \nabla\psi + q(\psi)\ \nabla\psi \times \nabla\theta \quad , \tag{5}$$

where $2\pi\psi$ is the poloidal flux within a magnetic surface, q is the safety factor, θ is the generalized poloidal angle, and ζ is the generalized toroidal angle. For axisymmetric equilibria, $\vec{B}$ can also be expressed as

$$\vec{B} = \nabla\phi \times \nabla\psi + g\nabla\phi \quad , \tag{6}$$

where ϕ is the toroidal angle in cylindrical (X,ϕ,Z) coordinates. Then, ζ is related to ϕ by

$$\zeta = \phi - q\ \delta(\theta,\psi) \quad , \tag{7}$$

where $\delta(\theta,\psi)$ is periodic in θ and is determined by

$$q\left(1 + \frac{\partial\delta}{\partial\theta}\right) = g\,\mathcal{J}/X^2 \quad , \tag{8}$$

with $\mathcal{J} = (\nabla\psi \times \nabla\theta\cdot\nabla\varphi)^{-1}$ being the Jacobian. The $\nabla\phi$ component of Eq. (1) gives

$$\vec{B}\cdot\nabla G = 0 \quad , \tag{9}$$

where $G(\psi) = \sigma g$, and $\sigma = 1 + (P_\perp - P_\parallel)/B^2$. The $\nabla\psi$ component of Eq. (1) leads to

$$\Delta^*\psi \equiv X^2\nabla\cdot\left(\frac{\nabla\psi}{X^2}\right) = -\frac{X^2}{\sigma}\left.\frac{\partial P_\parallel}{\partial\psi}\right|_B - \frac{GG'}{\sigma^2} - \frac{\nabla\psi\cdot\nabla\sigma}{\sigma} \quad , \tag{10}$$

which will be used to solve ψ if $P_\parallel(\psi,B)$, $G(\psi)$, and appropriate boundary conditions are specified. For isotropic equilibria, Eq. (10) reduces to the

Grad-Shafranov equation with $\sigma = 1$ and $G = g$.

Along a flux surface in the poloidal plane we have

$$\frac{ds}{d\theta} = \frac{\mathcal{J}|\nabla\psi|}{X} \quad , \tag{11}$$

where ds is the element of arc length along a constant (ϕ,ψ) line. Specification of $\mathcal{J}$ therefore, determines the θ coordinate. In this paper, we choose the Jacobian in the form

$$\mathcal{J}(X,Z) = \frac{X^i}{\alpha(\psi)|\nabla\psi|^j B^k} \quad , \tag{12}$$

where i,j,k can be freely specified and $\alpha(\psi)$ is given by the requirement that θ increases by 2π during one poloidal circuit. The form of $\mathcal{J}$ in Eq. (12) is a trivial generalization of that used in the PEST-2 code [6]. Thus, from Eq. (11) we have

$$\alpha(\psi) = \frac{2\pi}{\oint ds(|\nabla\psi|^{j-1}B^k/X^{i-1})} \tag{13}$$

For the choice $i = 2$, $j = k = 0$, the (ψ,θ,ζ) coordinate represents the PEST-1 coordinate. For $i = j = 1$, $k = 0$, we have the equal arc length coordinate system, and a Hamada-like coordinate system is obtained by letting $i = j = k = 0$. The choice $i = j = 0$, $k = 2$ is used for the Hamiltonian representation of the magnetic field [19].

The general flux coordinate system constructed here is not orthogonal and its metric is complicated because $\nabla\psi\cdot\nabla\zeta \neq 0$, $\nabla\theta\cdot\nabla\zeta \neq 0$, $\nabla\theta\cdot\nabla\psi \neq 0$, and $|\nabla\zeta|^2 \neq 1/X^2$. However, ζ is still an ignorable coordinate for axisymmetric equilibria, and the perturbed quantities can be represented by a single mode

varying as $\exp(-in\zeta)$.

III. Formulation of Eigenmode Equations

We will consider an axisymmetric toroidal plasma consisting of core and hot components with $\beta_h < \beta_c$ and $T_h >> T_c$. The ideal MHD description is adopted for the core plasma and the gyrokinetic description neglecting the Finite-Larmor-radius correction is employed for the hot component. Summing the collisionless equations of motion for each species, we obtain

$$\omega^2 \rho \vec{\xi} = \nabla \delta p_c + \nabla \cdot \delta \vec{p}_h + \vec{b} \times \vec{J} + \vec{B} \times (\nabla \times \vec{b}) \quad , \tag{14}$$

where $\vec{\xi}$ is the usual fluid displacement vector, $\vec{b}$ is the perturbed magnetic field, δp_c is the perturbed core plasma pressure, $\delta \vec{p}_h$ is the perturbed hot plasma pressure tensor, and ρ is the total plasma mass density. The following ideal MHD relations hold

$$\delta p_c + \vec{\xi} \cdot \nabla P_c + \gamma_s P_c \nabla \cdot \vec{\xi} = 0 \quad ,$$

$$\vec{b} = \nabla \times (\vec{\xi}_\perp \times \vec{B}) \quad ,$$

$$\delta \vec{E} = i\omega \vec{\xi} \times \vec{B} \quad , \tag{15}$$

where $\delta \vec{E}$ is the perturbed electric field, $\gamma_s = 5/3$, and P_c is the core plasma pressure. $\delta \vec{p}_h$ is obtained from the perturbed hot plasma distribution function

$$\delta F_h = \left[\frac{e\Phi}{m_h} \frac{\partial}{\partial \varepsilon} - \frac{\mu b_\parallel}{B} \frac{\partial}{\partial \mu}\right] F_{oh} + g_h \quad , \tag{16}$$

where g_h is governed by the gyrokinetic equation, with $g_h \sim \exp(-i\omega t)$,

$$[\vec{v}_\parallel \cdot \nabla - i(\omega - \omega_d)]g_h = -i(\tilde{\omega} - \omega_*^T)\frac{eF_{oh}}{T}\left[(\phi - \frac{v_\parallel A_\parallel}{c}) + \frac{m_h \mu b_\parallel}{e}\right], \tag{17}$$

where $\tilde{\omega} = -(T\omega/m_h)\partial \ell n F_{oh}/\partial \varepsilon$, $\omega_*^T = -i(T/m_h\omega_c)\hat{e}_B \times \nabla \ell n F_{oh} \cdot \nabla$, $\omega_d = -i\vec{v}_d \cdot \nabla$,

$\vec{v}_d = (\hat{e}_B/\omega_c) \times [\nabla \ell n B(\mu B) + \hat{K} v_\parallel^2]$, ϕ is the electrostatic potential, and $A_\parallel$ is the parallel vector potential. Since $\delta E_\parallel = 0$, we have $\omega A_\parallel/c = -i\hat{e}_B \cdot \nabla \phi$. For low-$\beta$ plasma we also have $\delta \vec{E}_\perp = -\nabla_\perp \phi$.

Considering MHD perturbations with frequencies much smaller than the hot particle transit and bounce frequencies, Eq. (17) can be readily solved for both the trapped and untrapped particles. For the untrapped particles

$$g_{hu} = \left(\frac{\tilde{\omega} - \omega_*^T}{\omega}\right)\frac{eF_{oh}}{T}\phi + O\left(\frac{\omega}{\omega_t}\right) \quad . \tag{18}$$

For the trapped particles, we have

$$g_{ht} = \left(\frac{\tilde{\omega} - \omega_*^T}{\omega}\right)\frac{eF_{oh}}{T}\left[\phi + \frac{\omega}{\omega - \langle\omega_d\rangle}\left\langle\frac{\omega_d \phi}{\omega} + \frac{m_h \mu b_\parallel}{e}\right\rangle\right] + O\left(\frac{\omega}{\omega_b}\right) \quad , \tag{19}$$

where $\langle A \rangle$ denotes the bounce average of A and is given by $\langle A \rangle = \oint A dl/|v_\parallel| / \oint dl/|v_\parallel|$. From Eqs. (16), (18), and (19), we obtain

$$\delta\tilde{p}_h = -\vec{\xi}_\perp \cdot \nabla\left[P_\perp \bar{I} + (P_\parallel - P_\perp)\hat{e}_B\hat{e}_B\right] + \delta\hat{p}_\perp \bar{I} + (\delta\hat{p}_\parallel - \delta\hat{p}_\perp)\hat{e}_B\hat{e}_B \quad , \tag{20}$$

where $\delta\hat{p}_\perp$ and $\delta\hat{p}_\parallel$ are due to trapped hot particles with

$$\begin{pmatrix}\delta\hat{p}_\perp \\ \delta\hat{p}_\parallel\end{pmatrix} = -\int_T d^3v \frac{\omega \frac{\partial F_{oh}}{\partial \varepsilon} + \frac{nm_h c}{e}\frac{\partial F_{oh}}{\partial \psi}}{\omega - \langle\omega_d\rangle}\left\langle \vec{\xi}_\perp \cdot \left[(\nabla \ell n B)\mu B + \hat{K} v_\parallel^2\right] + \mu b_\parallel \right\rangle \begin{pmatrix} m_h \mu B \\ m_h v_\parallel^2 \end{pmatrix}. \tag{21}$$

If we decompose the displacement vector as

$$\vec{\xi} = \frac{\xi_\psi \nabla\psi}{|\nabla\psi|^2} + \frac{\xi_s(\vec{B} \times \nabla\psi)}{B^2} + \frac{\xi_b \vec{B}}{B^2} \quad , \tag{22}$$

then after some complicated algebra, we obtain from Eqs. (14) and (15) the following set of two-dimensional integro-differential equations:

$$\begin{aligned}
\nabla\psi \cdot [\nabla \delta p_1 + \nabla \cdot \delta\vec{\vec{p}}_h] = {} & [\omega^2 \rho \xi_\psi + |\nabla\psi|^2 \vec{B} \cdot \nabla \left(\frac{\vec{B}\cdot\nabla\xi_\psi}{|\nabla\psi|^2}\right) \\
& + \frac{\nabla\psi}{B^2} \cdot \left[(2\vec{J}\times\vec{B} + \nabla B^2)\, P_c' + (\vec{J}\cdot\vec{B} - |\nabla\psi|^2 S)\, \frac{|\nabla\psi|^2}{B^2} S\right]\xi_\psi\Big] \\
& + \frac{\nabla\psi}{B^2} \cdot (2\vec{J}\times\vec{B} + \nabla B^2)\, \delta p_1 + (|\nabla\psi|^2 S - \vec{J}\cdot\vec{B})\, \frac{|\nabla\psi|^2}{B^2} \vec{B} \cdot \nabla\xi_s \\
& + \frac{\nabla\psi}{B^2} \cdot (2\vec{J}\times\vec{B} + \nabla B^2)\, \gamma_s P_c\, \nabla\cdot\vec{\xi} \quad ,
\end{aligned} \tag{23}$$

$$\begin{aligned}
\nabla\psi \cdot \nabla\xi_\psi = {} & - |\nabla\psi|^2 \left[\frac{\nabla\psi}{|\nabla\psi|^2} \cdot \left(\frac{\vec{J}\times\vec{B} + \nabla B^2}{B^2}\right) + \frac{P_c'}{B^2} + \nabla\cdot\left(\frac{\nabla\psi}{|\nabla\psi|^2}\right)\right]\xi_\psi \\
& - \frac{|\nabla\psi|^2}{B^2} \delta p_1 - |\nabla\psi|^2 \frac{\gamma_s P_c}{B^2} (\nabla\cdot\vec{\xi}) \\
& - |\nabla\psi|^2 \left[\frac{\vec{B}\times\nabla\psi}{B^2} \cdot \left(\frac{\vec{J}\times\vec{B} + \nabla B^2}{B^2}\right)\xi_s + \frac{\vec{B}\times\nabla\psi}{B^2} \cdot \nabla\xi_s + \nabla\cdot\left(\frac{\vec{B}\times\nabla\psi}{B^2}\right)\xi_s\right] \quad ,
\end{aligned} \tag{24}$$

$$\begin{aligned}
& \left[\omega^2 \rho \frac{|\nabla\psi|^2}{B^2} \xi_s + \vec{B} \cdot \nabla \left(\frac{|\nabla\psi|^2}{B^2} \vec{B}\cdot\nabla\xi_s\right)\right] - \gamma_s P_c \nabla \cdot \left(\frac{\vec{B}\times\nabla\psi}{B^2}\right) \nabla\cdot\vec{\xi} \\
& = \left[\nabla\cdot \left(\frac{\vec{B}\times\nabla\psi}{B^2}\right) \delta p_1 + \frac{\vec{B}\times\nabla\psi}{B^2} \cdot \nabla\delta p_1\right] + \left(\frac{\vec{B}\times\nabla\psi}{B^2}\right) \cdot \nabla\cdot\delta\vec{\vec{p}}_h \quad ,
\end{aligned} \tag{25}$$

$$\{(\frac{B^2+\gamma_s P_c}{B^2})\,\nabla\cdot\vec{\xi} + \frac{\vec{B}\cdot\nabla}{\omega_\rho^2}\,[\frac{\gamma_s P_c}{B^2}\,\vec{B}\cdot\nabla(\nabla\cdot\vec{\xi})]\} + (\frac{\vec{B}\times\nabla\psi}{B^2})\cdot(\frac{\vec{J}\times\vec{B}+\nabla B^2}{B^2})\xi_s$$

$$= -\frac{\delta p_1}{B^2} + \frac{\vec{B}\cdot\nabla}{\omega_\rho^2}\,[\frac{\vec{B}}{B^2}\cdot\nabla\cdot\delta\vec{p}_h] - [\frac{\nabla\psi}{|\nabla\psi|^2}\cdot(\frac{\vec{J}\times\vec{B}+\nabla B^2}{B^2}) + \frac{P_c'}{B^2}]\xi_\psi$$

$$+ \frac{\vec{B}\cdot\nabla}{\omega_\rho^2}\,[[P_c' - \frac{\nabla\psi}{|\nabla\psi|^2}\cdot(\vec{J}\times\vec{B})]\,\frac{\vec{B}}{B^2}\cdot\nabla\xi_\psi] \quad , \tag{26}$$

where $S = (\vec{B}\times\nabla\psi)/|\nabla\psi|^2\cdot\nabla\times(\vec{B}\times\nabla\psi/|\nabla\psi|^2)$ is the negative local shear, $P_c'=\partial P_c/\partial\psi$, $\delta p_1=\delta p_c+\vec{b}\cdot\vec{B}$, $\xi_\psi=\vec{\xi}\cdot\nabla\psi$, and $\xi_s=\vec{\xi}\cdot\vec{B}\times\nabla\psi/|\nabla\psi|^2$.

For anisotropic equilibria, $\vec{B}\cdot\nabla\cdot\delta\vec{p}_h$ contains $\partial\xi_\psi/\partial\psi$ and $\partial\xi_s/\partial\psi$ terms which are proportional to $(P_\parallel - P_\perp)_h$, and $(\vec{B}\times\nabla\psi)\cdot\nabla\cdot\delta\vec{p}_h$ contains only surface operators. But $\nabla\psi\cdot\nabla\cdot\delta\vec{p}_h$ contains all radial derivative terms $\partial\xi_\psi/\partial\psi$, $\partial\xi_s/\partial\psi$, $\partial\delta p_1/\partial\psi$, and $\partial(\nabla\cdot\vec{\xi})/\partial\psi$. The integral operators in Eqs. (23)-(26) are related to trapped particle bounce averages in the $\vec{B}$ direction. Since Eq. (25) does not have radial operators, Eqs. (23)-(26) are basically a third-order equation in $\partial/\partial\psi$. However, if the $(P_\parallel - P_\perp)_h$ terms can be neglected, such as in the case of low β_h (i.e., $\beta_h \ll \beta_c$), then Eq. (26) involves only surface operators and Eqs. (23)-(26) form a second-order equation in $\partial/\partial\psi$ as in the ideal MHD case. Equations (23)-(26) can be formally solved by inverting Eqs. (25) and (26) to obtain ξ_s and $\nabla\cdot\vec{\xi}$ in terms of δp_1 and ξ_ψ, and substituting them into Eqs. (23) and (24). This procedure is similar to that employed for the ideal MHD NOVA code. Equations (23) and (24) can now be combined to form a second-order equation in $\partial/\partial\psi$. In the following, we shall consider $\beta_h \ll \beta_c$ and neglect the pressure anisotropy terms, i.e., the $(P_\parallel - P_\perp)_h$ terms. These pressure anisotropy terms will be included in future work. Then, we have

$$\vec{B}\cdot\nabla\cdot\delta\vec{p}_h = \vec{B}\cdot\nabla(\delta\hat{p}_\parallel - \vec{\xi}_\perp\cdot\nabla P_{\parallel h}) - (\delta\hat{p}_\parallel - \delta\hat{p}_\perp)\,\frac{\vec{B}}{B}\cdot\nabla B \quad ,$$

$$(\vec{B}\times\nabla\psi)\cdot\nabla\cdot\delta\vec{p}_h = (\vec{B}\times\nabla\psi)\cdot\nabla(\delta\hat{p}_\perp - \vec{\xi}_\perp\cdot\nabla P_{\perp h}) + (\delta\hat{p}_\parallel - \delta\hat{p}_\perp)(\vec{B}\times\nabla\psi)\cdot\vec{K} \quad ,$$

$$\nabla\psi\cdot\nabla\cdot\delta\vec{p}_h = \nabla\psi\cdot\nabla(\delta\hat{p}_\perp - \vec{\xi}_\perp\cdot\nabla P_{\perp h}) + (\delta\hat{p}_\parallel - \delta\hat{p}_\perp)\nabla\psi\cdot\vec{K} \quad . \tag{27}$$

In a general flux coordinate system (ψ,θ,ζ), ζ is still an ignorable coordinate for axisymmetric equilibria and we represent the perturbed quantities by a single mode varying as $\exp(-in\zeta)$, where n is the toroidal mode number. In terms of the new velocity space coordinates $(\varepsilon,\Lambda,\sigma)$, we have

$$\int d^3v = \sum_\sigma \sqrt{2}\,\pi \int_0^\infty d\varepsilon\varepsilon^{1/2} \int_0^h \frac{d\Lambda}{h[1-\Lambda/h]^{1/2}} \quad ,$$

where $\sigma = \pm 1$, the pitch angle $\Lambda = \mu B_o/\varepsilon$, B_o is the vacuum magnetic field at $X = R$, and $h = B_o/B(\psi,\theta)$. On a flux surface, untrapped particles correspond to $0 \le \Lambda \le h_{min}(\psi)$, and trapped particles to $h_{min}(\psi) \le \Lambda \le h$ at a given θ, where $h_{min}(\psi) = \text{Min}\,[h(\theta,\psi)]$ on the ψ surface. The bounce-average magnetic drift frequency is

$$\langle\omega_d\rangle = \frac{nmc\varepsilon}{e}\left\langle \frac{[K_\psi + K_s(\nabla\psi\cdot\nabla\alpha)]}{|\nabla\psi|^2}\left(1 - \frac{\Lambda}{2h}\right) - \frac{p'c}{B^2}\frac{\Lambda}{h}\right\rangle \quad , \tag{28}$$

where $K_\psi = 2\vec{K}\cdot\nabla\psi$ and $K_s = 2\vec{K}\cdot(\vec{B}\times\nabla\psi)/B^2$. The perturbed trapped particle pressures are

$$\begin{pmatrix}\delta\hat{p}_\perp\\ \delta\hat{p}_\parallel\end{pmatrix} = -2^{3/2}\pi m_h \int_0^\infty d\varepsilon\varepsilon^{5/2} \int_{h_{min}}^h \frac{d\Lambda}{h(1-\Lambda/h)^{1/2}} \frac{\partial F_{oh}/\partial\varepsilon}{(\omega - \langle\omega_d\rangle)}$$

$$\times \left\langle(\omega - \hat{\omega}_*)\left[2\left(1-\frac{3\Lambda}{2h}\right)\vec{\xi}_\perp\cdot\vec{K} - \left(\frac{\Lambda}{h}\right)\nabla\cdot\vec{\xi}_\perp\right]\right\rangle \begin{pmatrix}\left(\frac{\Lambda}{h}\right)\\ 2\left(1-\frac{\Lambda}{h}\right)\end{pmatrix} \quad , \tag{29}$$

where

$$\hat{\omega}_* = i(\hat{e}_B \times \nabla F_{oh} \cdot \nabla)/[\omega_c(\partial F_o/\partial \varepsilon)] \quad .$$

The boundary condition at the magnetic axis is $\xi_\psi = 0$. For fixed boundary modes the boundary condition is $\xi_\psi = 0$ at the plasma-wall interface. For free boundary modes the boundary condition at the plasma-vacuum interface is given by $\vec{b}_v \cdot \nabla\psi = \vec{B} \cdot \nabla\xi_\psi$, where $\vec{b}_v$ is the vacuum magnetic field which must be solved from the divergence-free equation $\nabla \cdot \vec{b}_v = 0$.

IV. Numerical Methods

The eigenmode equations, Eqs. (23) - (26), are solved by the Galerkin method, where the eigenfunction is represented by a linear superposition of a finite subset of a complete set of basis functions. We first represent the perturbed quantities by a finite Fourier series in θ,

$$\vec{\xi}(\xi,\theta,\zeta) = \sum_m \vec{\xi}_m(\psi) \exp\,[i(m\theta - n\zeta)] \quad , \tag{30}$$

where the summation over m is truncated to a total number of L poloidal harmonics, and n is the toroidal mode number. The elimination of ξ_s and $\nabla\cdot\vec{\xi}$ proceeds by finding the algebraic Fourier matrix representation of the surface operators. Introducing the bracket notation for an operator E,

$$E_{m'm} \equiv \langle m'|E|m\rangle \equiv \frac{1}{2\pi}\oint d\theta\ [\exp(-im'\theta)]E[\exp(im\theta)] \quad , \tag{31}$$

Eqs. (25) and (26) reduce to

$$E_{m'm} \begin{pmatrix} \xi_s \\ \Delta\cdot\vec{\xi} \end{pmatrix}_m = F_{m'm} \begin{pmatrix} P_1 \\ \xi_\psi \end{pmatrix}_m \quad , \tag{32}$$

where E and F represent the poloidal operators of the left- and right-hand sides of Eqs. (25) and (26), respectively, and the Fourier indices m' and m have the same truncated domain. Note that the evaluation of the algebraic matrix operations, $E_{m'm}$ etc., involves convolutions that occur in evaluating operator products. To avoid aliasing errors, a larger truncated Fourier series domain than L, say L*, is imposed and is increased until the results are satisfactorily converged. $E_{m'm}$ can be inverted to obtain ξ_{sm} and $(\nabla\cdot\vec{\xi})_m$ in terms of δp_{1m} and $\xi_{\psi m}$ and then by eliminating δp_{1m} in favor of $\xi_{\psi m}$. Equations (23) and (24) are reduced to a set of L second order differential equations.

$$\frac{\partial}{\partial r} H^{(1)}_{m'm} \frac{\partial}{\partial r} \xi_m + H^{(2)}_{m'm} \frac{\partial}{\partial r} \xi_m + H^{(3)}_{m'm} \xi_m + \frac{\partial}{\partial r} [H^{(4)}_{m'm} \xi_m] = 0 \ , \tag{33}$$

where the H's are algebraic L × L matrices and are functions of r only, where $r = (\psi/\psi_{tot})^{1/2}$ and $\xi_m = \xi_{\psi m}(r)$ is a vector of dimension L. The explicit expressions of the H's are too tedious and complicated to present in full detail here. The boundary conditions at the magnetic axis are now modified to $\xi_m = 0$ for $m^2 \neq 1$ and $\partial\xi_m/\partial r = 0$ for $m^2 = 1$.

Equation (33) is integrated by employing cubic B-splines [7] to approximate the eigenfunction $\xi_m(r)$. The cubic spline has the advantageous property of minimum curvature among all third order polynomials [12]. For a given partition of N-grid points, $\Delta = \{r_1 < r_2 \ldots < r_N\}$, the function $\xi_m(r)$ is approximated by piecewise cubic polynomials in each subinterval (r_i, r_{i+1}). The polynomials and their first two derivatives are required to be

continuous at the grid points. Since a cubic polynomial is determined by four coefficients and there are N-1 intervals, there are a total of 4(N-1) unknowns to define a cubic spline function. There are 3(N-2) constraints at the (N-2) interior points so that the cubic spline function is determined by N+2 parameters. The most convenient cubic spline representation is the basis set of B-spline finite elements [13-15] $\{U_k | k=1,N+2\}$, which are local piecewise cubic polynomials occupying four grid intervals with continuity up to second-order derivatives and are shown in Fig. 1 for the uniform grid point case. It can be easily shown that every cubic spline can be expressed as a linear combination of B-spline elements. In order to define uniquely the N+2 B-spline elements, we assume that at each end of the grid partition there are three extra grid points extending outside the computational domain. This extended partition is unsatisfactory, and the problem is resolved by letting the exterior points coalesce at the end points, i.e., $r_{-2} = r_{-1} = r_0 = r_1$ and $r_{N+3} = r_{N+2} = r_{N+1} = r_N$. A typical set of cubic B-spline finite elements for a uniform grid partition is shown in Fig. 2(a), and Fig. 2(b) shows an example of cubic B-spline finite elements for a nonuniform grid partition.

The eigenfunction $\xi_m(r)$ is interpolated by the representation

$$\xi_m(r) \doteq \sum_{k=1}^{N+2} \xi_{m,k} U_k(r) \equiv S_m(r) \quad , \tag{34}$$

where $S_m(r)$ is the cubic spline approximation of $\xi_m(r)$. For the given values of $\xi_m(r)$ at the N-grid points, Eq. (34) is not uniquely defined because there are N+2 parameters $\xi_{m,k}$. Uniqueness is obtained by imposing two boundary conditions for $S_m(r)$, and in this paper we require that $\xi_m'(r) = S_m'(r)$ at the end grid points. To implement these two extra boundary conditions, we interpolate the first and the last four grid points by cubic Lagrange polynomials

$\tilde{S}_m(r)$ and require that $S_m'(r) = \tilde{S}_m'(r)$ at the end points $r = r_1$ and r_N[14]. At least for a uniform grid partition, this scheme preserves the asymptotic error scaling of N^{-4} [7,15] and has the advantage of not requiring extra four function evaluations.

Operating on Eq. (33) with the projection operator, $O_k = \int_0^1 dr\, U_k$ and interpolating the known functions $H^{(1)}$, $H^{(2)}$, $H^{(3)}$, and $H^{(4)}$ in terms of the same cubic B-spline finite elements, we obtain a set of algebraic equations:

$$\sum_{m,k} M_{mk}^{m'k'} \xi_{mk} = 0, \tag{35}$$

where

$$M_{mk}^{m'k'} = \sum_{j=1}^{N+2} \Big\{ h_{m'm}^{(1)j} \Big[U_j U_{k'} \Big|_0^1 - \int_0^1 (U_k, U_j' + U_{k'}, U_j)\, U_k'\, dr \Big] + h_{m'm}^{(2)j} \int_0^1 U_{k'}, U_j U_k'\, dr + h_{m'm}^{(3)j} \int_0^1 U_{k'}, U_j U_k\, dr \Big\},$$

and

$$H_{m'm}^{(1)} = \sum_{j=1}^{N+2} h_{m'm}^{(1)j}\, U_j(r), \text{ etc.} \tag{36}$$

Note $M_{mk}^{m'k'}$ is a $(N+2)L \times (N+2)L$ matrix with nonvanishing elements along its L^2 7-banded diagonals. After imposing the boundary conditions to modify the matrix M, the nontrivial solution of Eq. (35) can be obtained by requiring

$$f(\omega) \equiv \det|M(\omega)| = 0 \quad . \tag{37}$$

The eigenvalue problem is nonlinear in ω and its numerical solutions can be

found by iterative procedures. Convergence is assumed if $|[f(\omega_{p+1}) - f(\omega_p)]/f(\omega_p)| < \varepsilon_1$, and/or $|\omega_{p+1} - \omega_p| < \varepsilon_2$, where ε_1 and ε_2 are appropriate small numbers, and p denotes the iteration step. When the eigenvalue iteration is converged to the required accuracy, Eq. (35) is used to construct the eigenvectors $\vec{\xi}$ and P_1. For this purpose, the matrices of Eqs. (23)-(26) for each surface are saved in disk files when they are computed during the calculation of the matrix elements of $M_{mk}^{m'k'}$.

The iteration is computationally expensive because the matrix inversion must be carried out for Eqs. (25) and (26) at each iteration for each surface. Consequently, the execution time scales as the total number of radial grid points N as well as L^2 for the matrix inversion. Finally, to be consistent we have also employed cubic B-spline finite elements to obtain the equilibrium quantities from the mapping codes.

Next, we consider the vacuum solution of $\nabla\cdot\vec{b}_v = 0$ with the vacuum region surrounded by a conducting wall. For the $n\neq 0$ modes, we represent $\vec{b}_v = \nabla\chi$. Then in terms of the Green's theorem we have

$$2\pi\chi(\vec{x}_s) = \int d\vec{s}_t \cdot [G(\vec{x}_t|\vec{x}_s)\,\nabla_t\chi(\vec{x}_t) - \chi(\vec{x}_t)\nabla_t G(\vec{x}_t|\vec{x}_s)], \tag{38}$$

where we have chosen the Green's function G to satisfy

$$\nabla_t^2\, G(\vec{x}_t|\vec{x}_s) = 4\pi\delta(\vec{x}_t - \vec{x}_s) \quad , \tag{39}$$

and $G(\vec{x}_t|\vec{x}_s) = |\vec{x}_t - \vec{x}_s|^{-1}$. $\vec{x}_s$ can be either on the plasma-vacuum interface or on the wall, and the integral extends over both surfaces in Eq. (38). With the boundary conditions $\nabla\chi\cdot\nabla\psi = \vec{B}\cdot\nabla\xi_\psi$ on the plasma-vacuum interface and $\nabla\chi\cdot d\vec{s}_w = 0$ on the wall, Eq. (38) can be solved to obtain χ on both surfaces by

the method of collocation [20].

For the n = 0 mode, the magnetic field cannot be described by a single-valued scalar potential. Instead, we follow the procedure of Lüst and Martensen [21] and define

$$\vec{b}_v = \nabla\chi + a_1\nabla\phi \times \nabla\alpha + a_2\nabla\phi \quad , \tag{40}$$

where a_1 and a_2 are constants related to the perturbed quantities. χ can be obtained by the same procedure as for the $n \neq 0$ modes with the additional constraint $\oint \chi d\theta = 0$ due to the singular nature of the matrix in Eq. (38) for the n = 0 mode. α can be solved by taking $\nabla\phi \cdot \nabla \times \vec{b}_v = 0$ and we have

$$\Delta^* \alpha \equiv \nabla \cdot \left(\frac{\nabla\alpha}{X^2}\right) = 0 \quad . \tag{41}$$

The boundary conditions are $\alpha = 1$ on the plasma-vacuum interface and $\alpha = 0$ on the wall. Equation (41) again can be solved in terms of the Green's theorem

$$\frac{4\pi^2\alpha(\vec{x}_s)}{X_s} = \oint \frac{d\vec{s}_t}{X_t^2} \cdot \left[\hat{G}(\vec{x}_t|\vec{x}_s)\ \nabla_t\alpha(\vec{x}_t) - \alpha(\vec{x}_t)\nabla_t\hat{G}(\vec{x}_t|\vec{x}_s)\right] \quad , \tag{42}$$

where the Green's function $\hat{G}$ satisfies

$$\Delta_t^*\hat{G}(\vec{x}_t|\vec{x}_s) = -\frac{4\pi}{X_s^2}\,\delta(X_t - X_s)\delta(Z_t - Z_s) \quad , \tag{43}$$

and is given by

$$\hat{G}(\vec{x}_t|\vec{x}_s) = -\frac{4\pi X_t}{r}\,P^1_{-1/2}(w) \quad , \tag{44}$$

where $P^1_{-1/2}$ is the associated generalized Legendre function,

$$r = [(X_s^2 - X_t^2)^2 + (Z_s - Z_t)^4 + 2(X_s^2 + X_t^2)(Z_s - Z_t)^2]^{1/4} \quad , \tag{45}$$

and

$$w = \frac{[X_s^2+X_t^2+(Z_s-Z_t)^2]}{r^2} \quad . \tag{46}$$

To determine a_1 and a_2 we make use of the property

$$\int \nabla\chi \cdot \nabla\phi d^3x = \int \nabla\chi \cdot (\nabla\phi \times \nabla\alpha)d^3x = 0 \quad .$$

Then, with the aid of the boundary conditions $\vec{A} \times d\vec{s}_w = 0$ on the wall and $\vec{A} \times \nabla\psi = \xi_\psi \vec{B}$ on the plasma-vacuum interface, where $\vec{A}$ is the vector potential defined by $\vec{b}_v = \nabla \times \vec{A}$, we obtain

$$a_1 = \frac{\oint(\phi\times\nabla\alpha) \cdot (\hat{n}_p\times\vec{A})ds_p}{\int|\nabla\phi\times\nabla\alpha|^2 d^3x} \quad , \tag{47}$$

and

$$a_2 = \frac{\oint\nabla\phi\cdot(\hat{n}_p\times\vec{A})ds_p}{\int|\nabla\phi|^2 d^3x} \quad , \tag{48}$$

where s_p denotes the plasma surface and $\hat{n}_p = -\nabla\psi/|\nabla\psi|$. After we solve the vacuum magnetic field $\vec{b}_v$ in terms of ξ_ψ, we obtain the boundary condition for solving Eqs. (23)-(26) at the plasma-vacuum interface:

$$\delta p_1 = \vec{b}_v \cdot \vec{B} = \sum_{m,m'} \tilde{M}_{mm'} \xi_{\psi m'} \exp[i(m\theta - n\zeta)] \quad . \tag{49}$$

Note that $\delta p_\parallel$ is related to ξ_ψ and $\partial\xi_\psi/\partial\psi$ in Eqs. (23)-(24). This concludes our discussion on the vacuum solutions.

V. Convergence Studies

To illustrate the convergence properties of the NOVA code, we first consider the analytical Solovév equilibria [16] which have been used previously [17] for extensive comparisons of variational ideal MHD stability codes. Our ideal MHD results will be compared with the previous results, which provide a series of cross checks essential for validating such a large, complex code. The Solovév equilibria which satisfy the Grad-Shafranov equation, Eq. (10), for isotropic equilibria with $g' = 0$, are given by

$$\psi = \frac{\pi B_o}{ER^2 q(0)} \left[X^2 Z^2 + \frac{E^2}{4}(X^2-R^2)\right] , \tag{50}$$

$$P(\psi) = \frac{(1+E^2)B_o}{2\pi ER^2 q(0)} (\psi_B - \psi) , \tag{51}$$

$$q(\psi) = RB_o \oint \frac{ds}{X|\nabla\psi|} , \tag{52}$$

where (X,ϕ,Z) is a cylindrical coordinate system, B_o is the toroidal field at the magnetic axis $X = R$, $P(\psi)$ is the plasma pressure, and $q(\psi)$ is the safety factor with the contour of integration along a line of constant ψ and ϕ. The system is characterized by the following parameters: the ellipticity E, the inverse aspect ratio $\varepsilon \equiv [\psi_B q(o)/\pi ER^2 B_o]^{1/2}$, and $q(0)$. The wall position is specified by $\Lambda = (\psi_w/\psi_B)^{1/2}$, and $2\pi\psi_B$ is the total poloidal flux in the plasma.

To achieve the correct eigenvalue and an accurate representation of the

corresponding eigenfunction, in principle one requires a very large number of basis functions. Since this number is limited by the computer memory and computing time, it is necessary to extrapolate from the lower order representations to obtain the asymptotic eigenvalue. Fortunately, we need only a few points because the extrapolation formulas are simple.

Numerical convergence is shown below for the small aspect ratio, elliptical case with the parameters: $R = B_0 = 1$, $E = 2$, $\epsilon = 1/3$, $q(0) = 0.3$, $\Lambda = 1$, and $n = 2$. We employ a uniform r-mesh of N grid points and retain the poloidal harmonics $m = [-L_o, L_o]$. For the equal arc-length θ coordinate, the convergence curves of the eigenvalue ($\gamma^2 \equiv -\omega^2$) are shown in Fig.3. Here γ^2 is normalized in terms of $\omega_A^2 = B^2(0)/\rho(0)q^2(1)R^2$. The eigenvalue γ^2 scales as $\gamma^2 = \gamma_1^2 + C_1 \exp(-L_o/2)$ for fixed N and as $\gamma^2 = \gamma_2^2 + C_2 N^{-4}$ for fixed L_o, where γ_1^2 and γ_2^2 are the converged values for fixed N and L_o, respectively. The results from the PEST code show that γ^2 scales as $\gamma^2 = \gamma_3^2 + D_1 \exp(-L/2)$ for fixed N, where $L = 2L_o + 1$, and for fixed L, as $\gamma^2 = \gamma_4^2 + D_2 N^{-2}$. Note that if we use the PEST θ-coordinate, the growth rate from our code also scales as $\gamma^2 = \gamma_1^2 + \hat{C}_1 \exp(-L/2)$. Convergence curves from the PEST code are also shown in Fig. 3. Detailed comparison between the results of our code and those of the PEST code indicates that $|C_1| \sim |D_1|$ and $|C_2| \ll |D_2|$. Even with $N = 5$, our code converges in L_o with an error of less than 1% of its converged value. On the other hand, comparable accuracy from the PEST code would require at least three times as many linear finite elements. The eigenfunction ξ_ψ and the plasma flow pattern for this case are shown in Figs. (4a) and (4b), respectively. Comparisons of the converged values of the square of the growth rate from different Solovév equilibria obtained from various ideal MHD stability codes [17] are summarized in Table I. For most of the cases, our results are roughly between those of the PEST [1] and ERATO [2]

codes. These small discrepancies may be due to the different mapping codes used in these stability codes.

VI. Energetic Particle Effects on the Internal Kink Modes and Excitation of Fishbone Modes

The n=1 ideal MHD internal kink mode is usually unstable for tokamak plasmas with $\beta > \beta_{crit}$ and $q(0) < 1$ so that the $q = 1$ surface lies within the plasma. The growth rate of this mode is typically a factor of ϵ_o^2 smaller than the more dangerous external kink, where ϵ_o is the inverse aspect ratio. The stabilization of the internal kink and ballooning modes by an energetic particle component mirror-trapped on the unfavorable-curvature side of the tokamak has been proposed by Rosenbluth et al. [22] Their stabilization mechanism requires that the hot particles drift across field lines rapidly i.e., $\langle\omega_d\rangle >> |\omega|$ and $(\omega_*/\langle\omega_d\rangle) > 0$. The stabilizing kinetic energy of the hot particles may bring the plasma into the second stability region, where the stability may improve with increasing β. They also argue that when $\langle\omega_d\rangle$ is not large enough, marginal stability occurs with a real frequency close to $\langle\omega_d\rangle$. Chen et al. [18] further showed that for $\beta_h > \beta_{hcrit}$ and $(\omega_*/\langle\omega_d\rangle) >> 1$, the trapped energetic ions can resonantly destabilize a new branch of internal kink mode (called fishbone mode) with a real frequency comparable to $\langle\omega_d\rangle$ and that the growth rates are of the same order as the ideal internal kink values. This fishbone mode was used to explain the experimental observations of large amplitude bursts of m=n=1 MHD fluctuations in tokamak experiments with high-power, nearly perpendicular neutral beam injections.

These previous analytical theories [18,22] of energetic particle effects on the internal kink mode were performed for large aspect ratio tokamak plasmas with circular, concentric magnetic surfaces, and the radial plasma displacement ξ_r was taken as the cylindrical solution of the $m = n = 1$ mode

with ξ_r = constant for $q \leq 1$ (or $r \leq r_s$), and $\xi_r = 0$, otherwise. In addition, there are other approximations made in calculating energetic particle contributions to δW, such as, $1-q(0)=0$, $(\omega_*/\langle\omega_d\rangle) > 0$ for the whole minor radius, and no toroidal couplings of neighboring poloidal harmonics. Those approximations can be quite erroneous for realistic finite aspect ratio tokamaks. Therefore, the analytical theory, although it predicted the excitation of the fishbone mode, failed to give quantitative predictions of the critical β_h for both the stabilization of the internal kink and the excitation of the fishbone mode. Furthermore, when more realistic particle velocity distribution functions of the α particles are considered, the qualitative conclusions of the analytic theory may become invalid. In fact, the behavior of MHD modes depends strongly on both the energetic particle distributions and the plasma equilibria, and it is important to have a numerical code (e.g., NOVA-K code) that computes the stability of low-n MHD modes for realistic energetic particle distributions and plasma equilibria.

In this section we will present numerical studies of the effects of energetic particles on the n=1 internal kink mode by using the NOVA-K code. We will first establish the numerical convergence of the NOVA-K code. Then by comparing the numerical results with the analytical theory [18], we will point out the usefulness of the numerical calculations. We will assume $\beta_c >> \beta_h$, so that the equilibrium is approximately isotropic and is determined by the core component only. We first consider an equilibrium with circular plasma surface computed from a flux equilibrium code with the profiles $P_c(y) = P_o(1-y^2)^2$, $q(y) = q(0) + y([q(1) - q(0) + (y - 1)(q'(1) - q(1) + q(0))\ (1-y_s)/(y-y_s)/(y-y_s]$, where $y_s = [q'(1) - q(1) + q(0)]/[q'(0) + q'(1) - 2(q(1) - q(0))]$, $y = \psi/\Delta\psi$, $\Delta\psi = \psi_{lim} - \psi_o$, ψ_{lim} is evaluated at the limiter, and ψ_o is evaluated at the magnetic axis. The parameters are $\Delta\psi = 0.061$, $\langle\beta\rangle_{av} =$

0.625%, R = 1.43, R/a = 3.4, P_o = 0.018, q(0) = 0.8, q(1) = 2.85, q'(0) = 13.82 and q'(1) = 106.6, and $\langle\beta_{pol}\rangle = 2\langle P\rangle/\langle B_{pol}^2\rangle = 0.4278$. Figure 5 shows the flux surfaces of the equilibrium, and Figs. 6(a) - 6(c) show the radial dependencies ($r = (\psi/\Delta\psi)^{1/2}$) of the trapped particle pitch-angle space bounded by h_{min} and h_{max}, the hot particle diamagnetic drift frequency, and the bounce-averaged magnetic drift frequency $\langle\omega_d\rangle$ for $\Lambda_o = 1.1$, respectively. Also plotted in Fig. 6(a) is the curve of $\langle\omega_d\rangle = 0$. Between the $\Lambda = h_{max}(r)$ and $\langle\omega_d\rangle = 0$ curves, we have $\langle\omega_d\rangle < 0$, and between the $\langle\omega_d\rangle = 0$ and $\Lambda = h_{min}$ curves, $\langle\omega_d\rangle > 0$. Particles with $\Lambda < h_{min}$, are untrapped. For $\Lambda = h_{min}$ particles are barely trapped, and for $\Lambda = h_{max}$ particles are deeply trapped at θ=0. It is clear that for a given pitch angle Λ_o, $\langle\omega_d\rangle$ may change from being negative to positive as r changes, which means that $(\omega_*/\langle\omega_d\rangle)$ also varies from being positive to negative. If the trapped particles are destabilizing to a certain MHD mode for $(\omega_*/\langle\omega_d\rangle) > 0$ in a certain radial region, the trapped particles in the radial region with $(\omega_*/\langle\omega_d\rangle) < 0$ would be stabilizing. Thus, the net effect of hot trapped particles must be integrated over the entire hot particle population with proper weightings of different poloidal harmonics, which can only be achieved by numerical solution of nonvariational codes such as the NOVA-K code.

For ICRF-heated plasmas the energetic particle distribution is approximated by a Maxwellian in energy and a delta function in pitch angle Λ,

$$F_{oh}(\varepsilon,\Lambda,\psi) = n_h(\psi)\left(\frac{2\pi T_h}{m_h}\right)^{-3/2}\exp\left(-\frac{m_h\varepsilon}{T_h}\right)\delta(\Lambda-\Lambda_o) \quad , \tag{53}$$

where T_h is the hot particle temperature. For neutral-beam-heated plasmas, F_{oh} is taken as a slowing-down distribution in energy and a delta function in pitch angle, i.e.,

$$F_{oh}(\varepsilon,\Lambda,\psi) = \begin{cases} \dfrac{n_h(\psi)\ \delta(\Lambda-\Lambda_o)}{\varepsilon_c^{3/2} + \varepsilon^{3/2}} & , \quad \varepsilon \leq \varepsilon_b \ , \\ 0 & , \quad \varepsilon > \varepsilon_b \ , \end{cases} \tag{54}$$

where ε_b is the neutral beam injection energy, and ε_c is the cutoff energy where the beam ions lose an amount of energy to the core ions equal to that lost to electrons. For α-particles, we will employ the slowing-down distribution, Eq. (53), but with uniform pitch angle distribution, and ε_b is the α-particle born energy. It should be emphasized that the NOVA-K can calculate stability for numerical hot particle distributions obtained from Fokker-Planck code calculations. The flux surface-averaged hot particle density is typically of the order of 10^{-2} times the core density and T_h(or ε_b) ranges between 30 and 100 keV. $n_h(\psi)$ is assumed to have the same functional dependence as $P_c(\psi)$ for simplicity. Since both ω_* and $\langle\omega_d\rangle$ are proportional to T_h or (ε_b), we will introduce a temperature scaling factor C_T in ω_* and $\langle\omega_d\rangle$. If $C_T \to 0$, $\omega_{*h} = \langle\omega_d\rangle = 0$ and the eigenmode equations, Eqs. (23) - (26), correspond to the Kruskal-Oberman energy principle [23]. For $C_T \to \infty$, Eqs. (23) - (26) correspond to the case studied by Rosenbluth et al.[22]. From Eq. (29), we see that both $\delta\hat{p}_\perp$ and $\delta\hat{p}_\parallel$ are proportional to $n_h(\psi)T_h$. Therefore, we will set $n_h(\psi)T_h = \alpha_h P_c(\psi)$ and vary α_h to change the hot particle pressure.

In the absence of energetic particles (α_h=0), the n = 1 fixed boundary ideal MHD internal kink mode is unstable with the growth rate $\gamma/\omega_A = 1.195 \times 10^{-2}$. Because the eigenfunction ξ_ψ has a sharp radial variation near the q=1 surface, the computation was carried out by using a spatially tailored r-grid with dense grid packing near the q = 1 surface. Since the poloidal harmonics

of ξ_ψ are dominated by $1 \le m \le 3$, we will use the equal arc-length θ coordinate and keep 7 poloidal harmonics $m = [-2,4]$ in the computation to ensure convergence in m. We have also checked the numerical convergence in radial grid points by using N=50, 75, and 100 to obtain the converged growth rate. Figure 7 shows the poloidal component of the eigenfunction ξ_ψ versus r; the q-profile is also shown in Fig. 7.

In the following, we will present the results of the neutral-beam-injected energetic particles on the stability of the n=1 internal kink modes and compare these results with the model dispersion relation calculation. The hot particle distribution is given by Eq. (54) with $\varepsilon_c = 0$, and $n_h(\psi)$ is taken to have the same ψ dependence as $p(\psi)$. The other fixed parameters for the energetic particles are $\varepsilon_b/T_c(0) = 10$, $R/\rho_h(0) = 100$, $m_h/m_c = 1$, $C_T = 1$, $\Lambda_o = 1.1$, where m_c and m_h are the core and hot ion mass, respectively, $\rho_h(0)$ is the hot ion gyroradius at the magnetic axis, and Λ_o is the pitch angle of the injected beam ions. For this equilibrium, the volume-averaged hot particle beta, $\beta_h \equiv 2\langle p_h\rangle/\langle B^2\rangle$, is related to the total volume-averaged beta, $\beta = 2\langle p\rangle/\langle B^2\rangle$, by $\beta_h = 1.38\,\alpha_h\beta$ where $\beta = 0.625\%$. In varying β_h (or α_h) we will keep the total β fixed so that as β_h is increased, the core plasma β_c is decreased by the same amount. Figure 8(a) shows the α_h dependence of the growth rates, γ/ω_A, of the ideal and the resonant fishbone branches of internal kinks. The computations were carried out by performing convergence studies with N = 50, 75, and 100 nonuniform radial grid points. We see that the N=100 case gives approximately the converged solutions. For the ideal branch, the eigenfunction ξ_ψ becomes increasingly singular as $\alpha_h > 0.035$. For the resonant branch, ξ_ψ becomes more singular as $\alpha_h < 0.07$. One also realizes that the solutions with singular ξ_ψ cannot be trusted because our cubic B-spline finite elements do not give proper representation of the singular ξ_ψ.

This is the most difficult problem in attempting the numerical solutions of MHD modes near marginal stability with $|\gamma/\omega_r| \ll 1$ or $|\gamma/\omega_A| \ll 1$ when the eigenfunction ξ_ψ becomes singular. The common practice of obtaining the behavior of the eigenvalue ω $(=\omega_r+i\gamma)$ near marginal stability is to extrapolate from the ω with well-behaved eigenfunctions. The two broken curves in Fig. 8(a) show the extrapolated values of γ near marginal stabilities of the ideal and the resonant branches of the internal kink modes. We can now conclude from Fig. 8(a) that the ideal branch of internal kink mode is stabilized by the injected energetic particles for $\beta_h > \beta_{h1} \equiv 0.031\%$ $(\alpha_h \equiv 0.036)$, but for $\beta_h > \beta_{h2} \equiv 0.0517\%$ $(\alpha_h \equiv 0.06)$ the fishbone branch of internal kink mode is resonantly destabilized by the injected energetic particles. Figure 8(b) shows the negative real frequency, $-(\omega_r/\omega_A)$, versus α_h for the corresponding cases of Fig. 8(a). As $\alpha_h \to 0$, the real frequency of the resonant branch evolves into a slow sound mode of the continuous spectrum, which is below the shear Alfvén continuous spectra. Note that the shear Alfvén continuous spectrum does not go to zero at the q=1 surface due to finite values of β and the surface component of the magnetic curvature [10]. It is the m=1 slow sound branch of the continuous spectrum that goes to zero frequency at the q=1 surface and determines the singular behavior of the n=1 internal kink mode near marginal stability.

In Figs. 9(a) and 9(b), the growth rates and the negative real frequencies, respectively, versus the hot particle pressure scaling factor α_h are plotted for several values of the hot particle injection energy scaling factor C_T. The fixed parameters are the same as in Fig. 8. For $C_T \leq 0.4$, the hot particle pressure is stabilizing for small values of α_h, but becomes destabilizing as α_h becomes larger $(\alpha_h > 0.036)$. The destablizing effect is accompanied by an increase in $|\omega_r|$ and is associated with $\omega - \langle\omega_d\rangle \to 0$

resonance. However, when C_T becomes larger with $C_T \simeq 1$, the ideal branch is stabilized for $\alpha_h \gtrsim \alpha_{h1} \simeq 0.036$ (for $C_T=1$). But the resonant fishbone branch is destabilized for $\alpha_h > \alpha_{h2} \simeq 0.06$ for $C_T \simeq 1$. For larger C_T, α_{h1} is smaller, but α_{h2} becomes larger. Note that the broken curves in Fig. 9(a) are obtained by employing the extrapolation scheme described in Fig. 8.

The results presented in Figs. 9(a) and 9(b) are qualitatively similar to those obtained from the following analytical dispersion relation [18] for the neutral-beam-injected energetic particle distribution given by Eq. (54):

$$-i\left(\frac{\omega}{\omega_A}\right) = \left(\frac{\gamma_{MHD}}{\omega_A}\right) - \frac{9}{8}\hat{\beta}_h\left[\frac{\omega_*}{\omega_d} + \frac{\omega}{\omega_d}\left(\frac{\omega_*}{\omega_d} - 1\right)\left[\ell n\left(1-\frac{\omega_d}{\omega}\right) + i\pi\sigma\right]\right] , \qquad (55)$$

where $0 < \mathrm{Re}(\omega) < \omega_d$, $\sigma = 0$ for $\mathrm{Im}(\omega) > 0$, $\sigma = 1$ for $\mathrm{Im}(\omega) = 0$, and $\sigma=2$ for $\mathrm{Im}(\omega) < 0$. ω_* and ω_d are the typical hot particle diamagnetic drift frequency and the bounce-averaged magnetic drift frequency, respectively. γ_{MHD} is the ideal MHD growth rate in the absence of hot particles, and $\hat{\beta}_h$ is proportional to the hot particle β_h. Equation (55) predicts that if $\gamma_{MHD} > 0$, the ideal branch will be stabilized for $\hat{\beta}_h > \hat{\beta}_{h1}$, where $\hat{\beta}_{h1} = (8\gamma_{MHD}\omega_d/9\omega_A\omega_*)$. At $\hat{\beta}_h \simeq \hat{\beta}_{h1}$, $\omega = 0$. The resonant fishbone branch will be destabilized for $\hat{\beta}_h > \hat{\beta}_{2h}$, where $\hat{\beta}_{h2} = 8\omega_d/[9\pi\omega_A(\omega_*/\omega_d - 1)]$. At $\hat{\beta}_h = \hat{\beta}_{h2}$, ω is purely real. Figure 10(a) shows the growth rate and Fig. 10(b) the real frequency for the fixed parameter $\omega_*/\omega_d = 10$. Several values of $\bar{\omega}_d \equiv \omega_d/\gamma_{MHD}$ are used. The curves labeled $\bar{\omega}_d \geq 3$ correspond to the ideal branch. We see that for $(\omega_*/\gamma_{MHD}) \geq \pi(\omega_*/\omega_d - 1)$ (i.e., $\beta_{h1} > \beta_{h2}$), the ideal branch is unstable for all β_h. For $\hat{\beta}_{h1} < \hat{\beta}_{h2}$, there is a stability window for $\hat{\beta}_{h1} \leq \hat{\beta}_h \leq \hat{\beta}_{h2}$. Figure 10(a) clearly shows these behaviors through the variations in $\bar{\omega}_d$ with ω_*/ω_d being held fixed. We should note that the real frequency shown in Fig. 10(b) is somewhat different from Fig. 9(b) for the resonant branch in the limit $\alpha_h \lesssim$

α_{h2}. This is because the analytical dispersion, Eq. (55), does not describe the MHD continuous spectrum that is contained in the NOVA-K code. The above comparison clearly demonstrates that the NOVA-K code gives correct results of the energetic particle effects on the n=1 internal kink mode.

Next, we examine the validity of the approximations made in the analytical theory of Chen et al.[18] Our calculations show that although the analytical theory gives qualitatively correct results, it fails to provide the correct values of the critical hot particle betas for both the stabilization of the ideal branch and the destabilization of the resonant fishbone branch. To make comparisons on the values of critical β_h, we impose similar approximations, as done in Ref. 18 in computing the perturbed hot particle pressures $\delta\hat{p}_\perp$ and $\delta\hat{p}_\parallel$ defined by Eq. (9), by retaining only the m=1 poloidal harmonics and taking 1-q(0) = 0. For the same parameters as in Figs. 8(a) and 8(b), the computed eigenvalues ω versus β_h are shown in Fig. 11. By comparing Figs. 8 and 11, we see that the qualitative behavior of the n=1 mode with analytical approximations is quite similar to that of Fig. 8 obtained without approximations. However, the horizontal β_h scale of Fig. 11 is about a factor of 4 smaller than that of Fig. 8. Thus, the analytical approximations have produced an error in β_{h1} and β_{h2} by roughly a factor of 4 in this particular example. The error is mainly due to the omission of higher poloidal harmonics in $\delta\hat{p}$. As seen in Fig. 7, the amplitudes of the m=2 and 3 are not negligible outside the q=1 surface. Also from Fig. 6 with Λ = 1.1, $(\omega_*/\langle\omega_d\rangle) < 0$ for r > 0.85, and thus the m=2,3 harmonics have opposite contributions to stability from the m=1 harmonic. This calculation tells us that we must employ the NOVA-K code to compute the correct values of the critical β_{h1} and β_{h2}.

Another important conclusion from the calculations of the NOVA-K code, that is different from that of the analytical theory, is that a necessary

condition to excite the resonant fishbone mode is $\beta > \beta_c$, where β_c is the ideal MHD critical β for the n=1 internal kink. It can be easily seen from the analytical dispersion relation, Eq. (55), that the critical β_{h2} is independent of γ_{MHD}, and there is no constraint on the total plasma β. Our conclusion is derived by computing the stabilities of several equilibria with decreasing β. As β is decreased, the growth rates of both the ideal branch and the resonant fishbone branch also decrease. For $\beta \leq \beta_c$, no instabilities are found by the NOVA-K code.

VII. Summary and Conclusion

In this paper we have presented a nonvariational MHD stability code (NOVA) which provides accurate and efficient numerical solutions of the magnetohydrodynamic stability of axisymmetric toroidal plasmas. In a general flux coordinate system (ψ,θ,ζ) the code makes use of cubic B-spline finite elements in the minor radius ψ direction and Fourier expansions in the poloidal θ and toroidal ζ directions. The ideal MHD eigenmode equations are reduced to a set of coupled second-order differential equations in the ψ direction. With the cubic B-spline finite elements, the problem is reduced to solving a matrix equation with nontrivial solutions. Extensive comparisons with existing variational codes [1-6] show that the ideal version of the NOVA code can produce more accurate results with less computational effort.

Since the NOVA code does not rely on the variational energy principle, this successful nonvariational approach has been extended to physical problems where the eigenmode equations are non-Hermitian, such as resistive MHD [24] and kinetic MHD. In this paper, we have also presented the NOVA-K code which integrates a set of non-Hermitian integro-differential equations due to energetic particles by the cubic B-spline finite element methods. Energetic

particle dynamics are governed by gyrokinetic equations and have significant effects on the stability of low frequency MHD modes. We have studied the problems of energetic particle stabilization of the n=1 internal kink mode and the excitation of the resonant fishbone modes by resonating with the trapped energetic particle magnetic drifts. Extensive comparisons with the results of the analytical dispersion for energetic particle distribution with single pitch angle have shown that, although the analytical results are qualitatively correct, they give incorrect values of critical β_h, which can be an order of magnitude different from those computed by the NOVA-K code. In addition, the results of the NOVA-K code indicate that a necessary condition for the excitation of the resonant fishbone mode is $\beta > \beta_c$, where β is the total plasma beta and β_c is the critical beta for the n=1 internal kink instability. This necessary condition is not predicted by the analytical dispersion relation.

Finally, the NOVA-K code has been employed to study the energetic particle effects on the internal kinks, external kinks, and toroidicity-induced shear Alfvén waves for various types of MHD equilibria and energetic particle distributions. For example, our results show that the α-particle distribution, which is uniform in pitch angle, has very little effect on the n=1 internal kink mode of Compact Ignition Tokamak (CIT) type equilibria. This is contrary to the results of several analytical calculations which either made a very improper approximation of keeping only the m=1 poloidal harmonic or failed to integrate over the α-particle pitch angle with self-consistent equilibria. Therefore, we believe that the NOVA-K code is an indispensable tool for studying the energetic particle effects on the MHD modes. The results of these studies will be presented in future publications.

ACKNOWLEDGMENTS

The author would like to thank Dr. L. Chen for valuable discussions. This work was supported by U.S. DoE Contract No. DE-AC02-76-CH03073.

REFERENCES

[1] R.C. Grimm, J.M. Greene, and J.L. Johnson, Meth. Comput. Phys., 16, (1976), 253.

[2] R. Gruber, F. Troyon, D. Berger, L.C. Bernard, S. Rousset, R. Shreiber, W. Kerner, W. Schneider, and K.V. Roberts, Comput. Phys. Comm. 21 (1981), 323.

[3] W. Kerner, Nucl. Fusion 16 (1976), 643.

[4] L.C. Bernard, F.J. Helton, and R.W. Moore, Comput. Phys. Comm. 24 (1981), 377.

[5] L.M. Degtyarev, V.V. Drozdov, A.A. Martynov, and S. Yu. Medvedev, Proceedings of International Conference on Plasma Physics, Lausanne, Switzerland, 1985, Vol. I, pp. 157-175.

[6] R.C. Grimm, R.L. Dewar, and J. Manickam, J. Comput. Phys. 49 (1983), 94.

[7] C.Z. Cheng and M.S. Chance, J. Comput. Phys. 71 (1987), 124.

[8] I.B. Bernstein, E.A. Frieman, M.D. Kruskal, and R.M. Kulsrud, Proc. Roy. Soc., Ser. A 244 (1958), 17-40.

[9] K. McGuire, et al., Phys. Rev. Lett. 50 (1983), 891; D. Johnson et al., in Proceedings of the Ninth International Conference on Plasma Physics and Controlled Nuclear Fusion Research, Baltimore, 1982 (IAEA, Vienna, 1983).

[10] C.Z. Cheng and M.S. Chance, Phys. Fluids 29 (1986), 3695.

[11] C.Z. Cheng, L. Chen and M.S. Chance, Ann. Phys. (NY) 161, (1984), 21.

[12] K.S. Kunz, Numerical Analysis (McGraw-Hill, New York, 1957), pp. 100-103.

[13] C. De Boor, J. Approx. Theory 6 (1972), 50.

[14] B.K. Swartz and R. S. Varon, J. Approx. Theory 6 (1972), 1.

[15] G. Strang and G.J. Fix, An Analysis of the Finite Element Method (Prentice-Hall, Inc., Englewood Cliffs, N.J. 1973), pp. 116-118.

[16] L.S. Solovév, Soc. Phys. JETP 26 (1968), 400.

[17] M.S. Chance, J.M. Greene, R.C. Grimm, J.L. Johnson, J. Manickam, W. Kerner, D. Berger, L.C. Bernard, R. Gruber, and F. Troyon, J. Comput. Phys. 28 (1978), 1.

[18] L. Chen, R.B. White, and M.N. Rosenbluth, Phys. Rev. Lett 52 (1984), 1122; R.B. White, L. Chen, R. Romanelli, and R. Hay, Phys. Fluids 28 (1985), 278.

[19] A.H. Boozer, Phys. Fluids 23 (1980), 904 and 26 (1985), 496; R.B. White and M.S. Chance, Phys. Fluids 27 (1984), 2455.

[20] M.S. Chance, R.L. Dewar, A.M.M. Todd, J. Manickam, R.C. Grimm, J.M. Greene, and J.L. Johnson, in Proceedings of the 8th International Conference on Numerical Simulation of Plasmas, June 28-30 (1978) PC-5: M.S. Chance and C.Z. Cheng, in Proceedings of the 11th International Conference on Numerical Simulation of Plasmas, June 25-27 (1985), 2.B.05.

[21] R. Lust and E. Martensen, Z. Naturforsch. A15 (1960), 706.

[22] M.N. Rosenbluth, S.T. Tsai, J.W. Van Dam, and M.G. Engquist, Phys. Rev. Lett. 51 (1983), 1967.

[23] M.D. Kruskal and C. Oberman, Phys. Fluids 1 (1958), 275.

[24] T.R. Harley, C.Z. Cheng, and S.C. Jardin, Bull. Am. Phys. Soc. 32 (1987), 1773.

TABLE 1

Comparison of the Eigenvalues γ^2 for Different Solovév Equilibria from Various Ideal MHD Stability Codes

ε	E	A	q(0)	q(a)	n	Kerner	PEST-1	ERATO	Degtyarev	NOVA
1/6	1	2	1.791	2.0	1	0.202	0.204		0.211	0.208
1/6	1	2	2.2387	2.5	1	0.504	0.506		0.511	0.508
1/3	2	1	0.3	0.5224	2	0.413	0.427	0.431	0.430	0.430
1/3	2	1	0.7	1.219	2	0.118	0.119	0.120	0.121	0.119
1/3	2	∞	1.2	2.0897	1		0.75	0.78		0.748
1/3	2	∞	2.0	3.4829	1		0.68	0.75		0.656
1/3	2	∞	0.6	1.0449	2		1.31	1.40	1.32	1.35
1/3	2	∞	1.0	1.7415	2		1.03	1.07	1.06	1.038

Figure Captions

Fig. 1 Typical cubic B-spline finite element for a uniform grid.

Fig. 2 Cubic B-spline finite elements for uniform and nonuniform partitions.

Fig. 3 Comparisons of convergence results in both the radial and the poloidal directions for our nonvariational code and the PEST code. The Solovév equilibrium has the parameters $R = B_o = 1$, $E = 2$, $\epsilon = 1/3$, $q(0) = 0.3$, $\Lambda = 1$, and $n = 2$. The eigenvalue γ^2 is extrapolated numerically in both the number of poloidal harmonics and the number of radial finite elements.

Fig. 4 (a) The poloidal harmonics of the eigenfunction ξ_ψ versus r, (b) the projection of the displacement vector onto the $\phi = 0$ plane for the converged solution as shown in Fig. 3. The q-profile is also shown in Fig. (3a).

Fig. 5 The flux surfaces of a circular tokamak equilibrium with average beta $\beta = 0.625\%$, $q(0) = 0.8$, $q(1) = 2.85$, $R/a = 3.4$, $R = 1.43$.

Fig. 6 (a) The radial variations of the trapped particle pitch angle Λ space bounded by h_{max} and h_{min}. The bounce average magnetic drift frequency $\langle\omega_d\rangle = 0$ curve is also shown, and above the $\langle\omega_d\rangle = 0$ curve, the hot ion $\langle\omega_d\rangle$ is negative for the $n = 1$ mode. $\Lambda = h_{max}$ corresponds to deeply trapped particles and $\Lambda = h_{min}$ corresponds to barely trapped particles. (b) The hot ion diamagnetic drift

frequency ω_{*h} versus r for the m = 1 poloidal harmonic. (c) The hot ion bounce-averaged magnetic drift frequency $\langle\omega_d\rangle$ versus r for Λ = 1.1, n=1.

Fig. 7 The poloidal components of the converged n = 1 fixed boundary internal kink mode eigenfunction ξ_ψ versus r. It is computed with an equal arc length θ-coordinate for the equilibrium described in Fig. 5. The eigenvalue is γ = 0.01195 and the q-profile is also shown.

Fig. 8 (a) The growth rates, (γ/ω_A), of both the ideal branch (I.B.) and the resonant fishbone branch (R.B.) versus α_h for the equilibrium described in Fig. 5. The total β is fixed and the hot particle slowing-down distribution is chosen with Λ_o = 1.1, ε_b/T_o = 10, $R/\rho_h(0)$ = 100, m_h/m_o = 1, C_T = 1, and thus the volume-averaged β_h = $1.38\alpha_h\beta$ with β = 0.625%. The broken curves represent the extrapolated growth rates near marginal stability. (b) The corresponding negative real frequencies, $-(\omega_r/\omega_A)$, versus α_h.

Fig. 9 (a) The growth rates, (γ/ω_A), versus α_h for both the ideal and the resonant branches for several values of C_T which scales $\langle\omega_d\rangle$ and ω_*. The fixed parameters are the same as in Fig. 8. (b) The corresponding negative real frequencies, $-(\omega_r/\omega_A)$, versus α_h.

Fig. 10 (a) The growth rates γ/γ_{MHD} computed from the analytical dispersion expression, Eq. (55), versus $\hat{\beta}_h$ for several values of $\bar{\omega}_D$ = $\langle\omega_d\rangle/\gamma_{MHD}$. The curve labelled with $\bar{\omega}_D \geq 3$ represents the ideal branch. (b) The corresponding real frequencies (ω_r/γ_{MHD}) versus $\hat{\beta}_h$.

Fig. 11 The growth rates, (γ/ω_A), and negative real frequencies, $-(\omega_r/\omega_A)$, of both the ideal and the resonant branches versus α_h for the same equilibrium and fixed hot particle parameters as in Fig. 8. The computations are performed with analytical approximations when computing $\hat{\delta p}_\perp$ and $\hat{\delta p}_\parallel$ defined by Eq. (29).

#85T0198

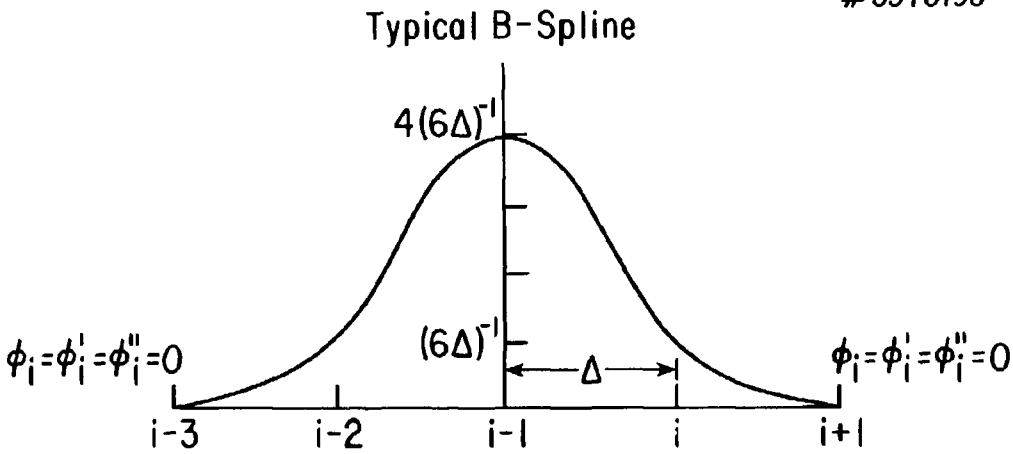

Fig. 1

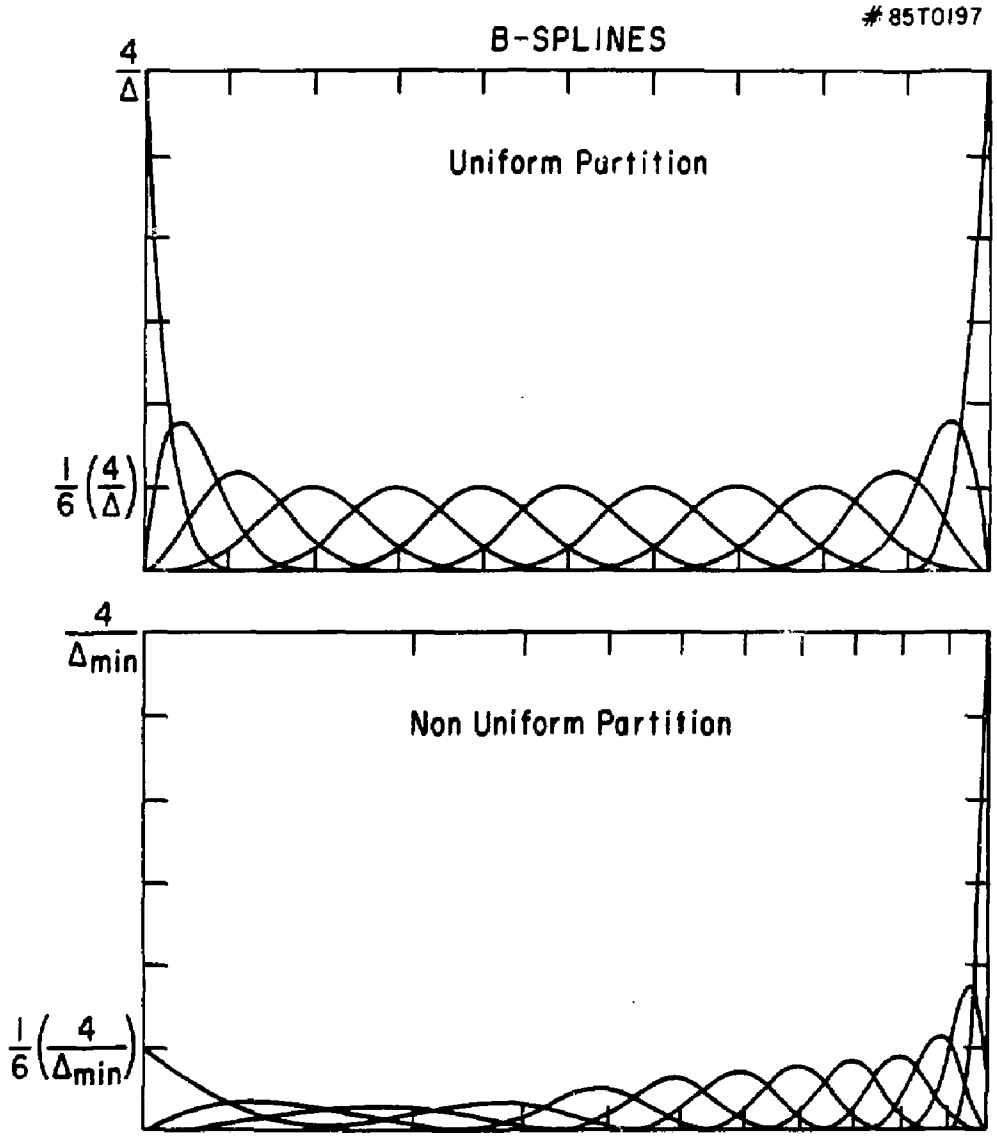
#85T0197
B-SPLINES
4/Δ
Uniform Partition
1/6 (4/Δ)
4/Δmin
Non Uniform Partition
1/6 (4/Δmin)

Fig. 2

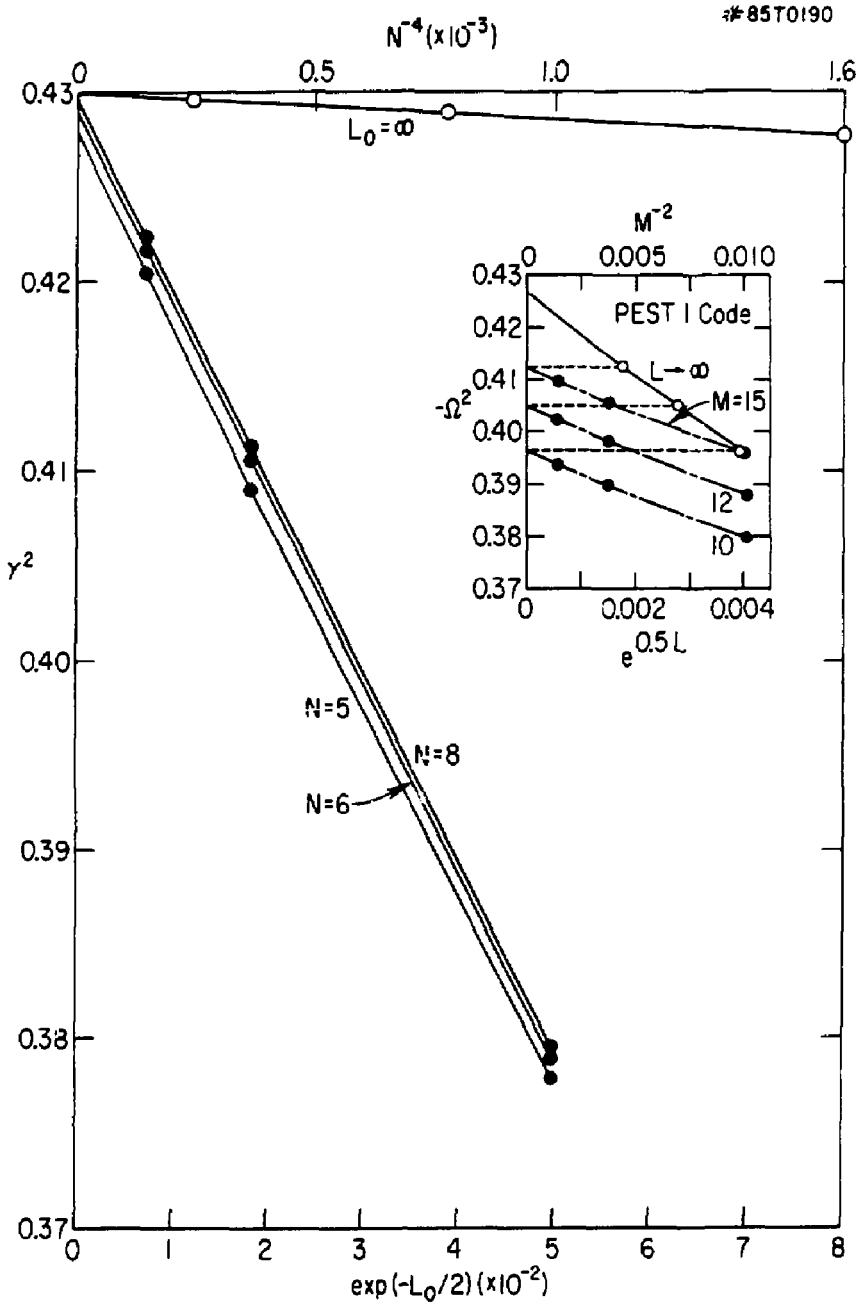
#85T0190
$N^{-4}(x10^{-3})$
0
0.5
1.0
1.6
0.43
$L_0=\infty$
0.42
0.41
γ^2
0.40
0.39
0.38
0.37
N=5
N=8
N=6
0
1
2
3
4
5
6
7
8
$\exp(-L_0/2)(x10^{-2})$
M^{-2}
0
0.005
0.010
PEST I Code
$L\to\infty$
M=15
12
10
$-\Omega^2$
0.002
0.004
$e^{0.5L}$

Fig. 3

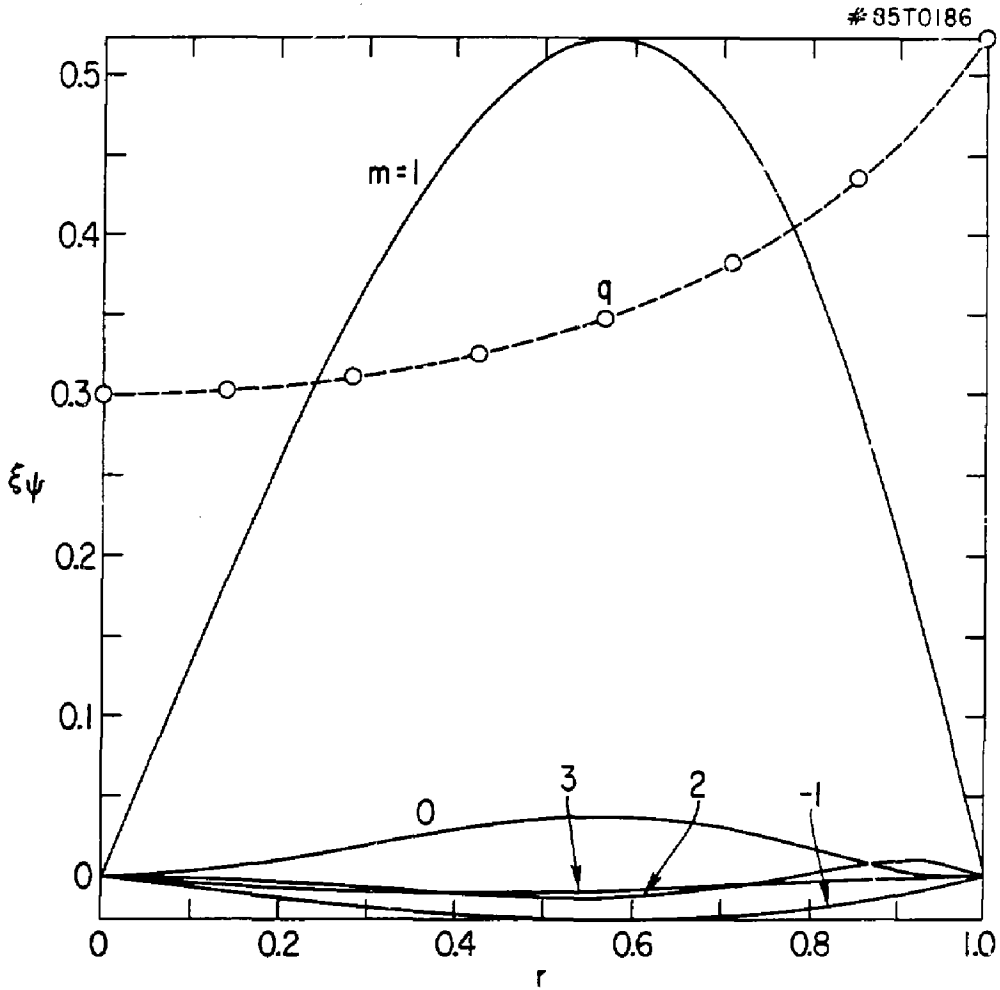

Fig. 4(a)

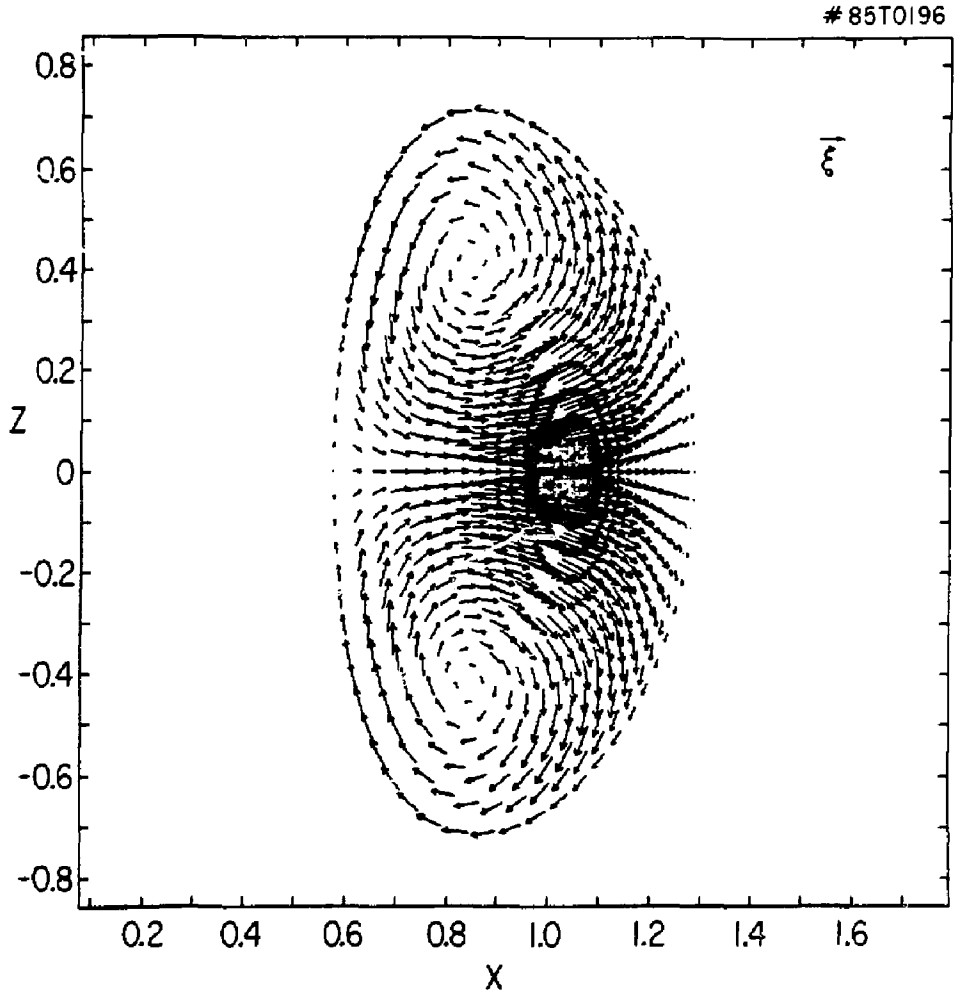

Fig. 4(b)

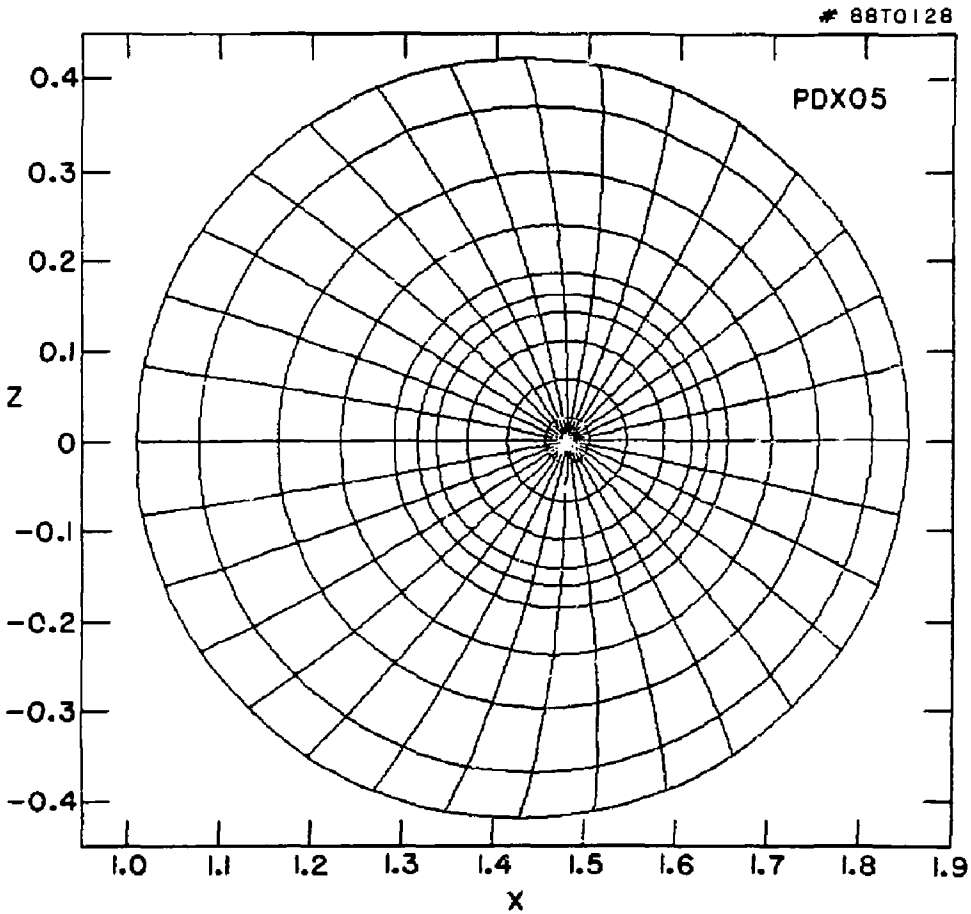
88T0128
PDX05
0.4
0.3
0.2
0.1
Z
0
-0.1
-0.2
-0.3
-0.4
1.0
1.1
1.2
1.3
1.4
1.5
1.6
1.7
1.8
1.9
X

Fig. 5

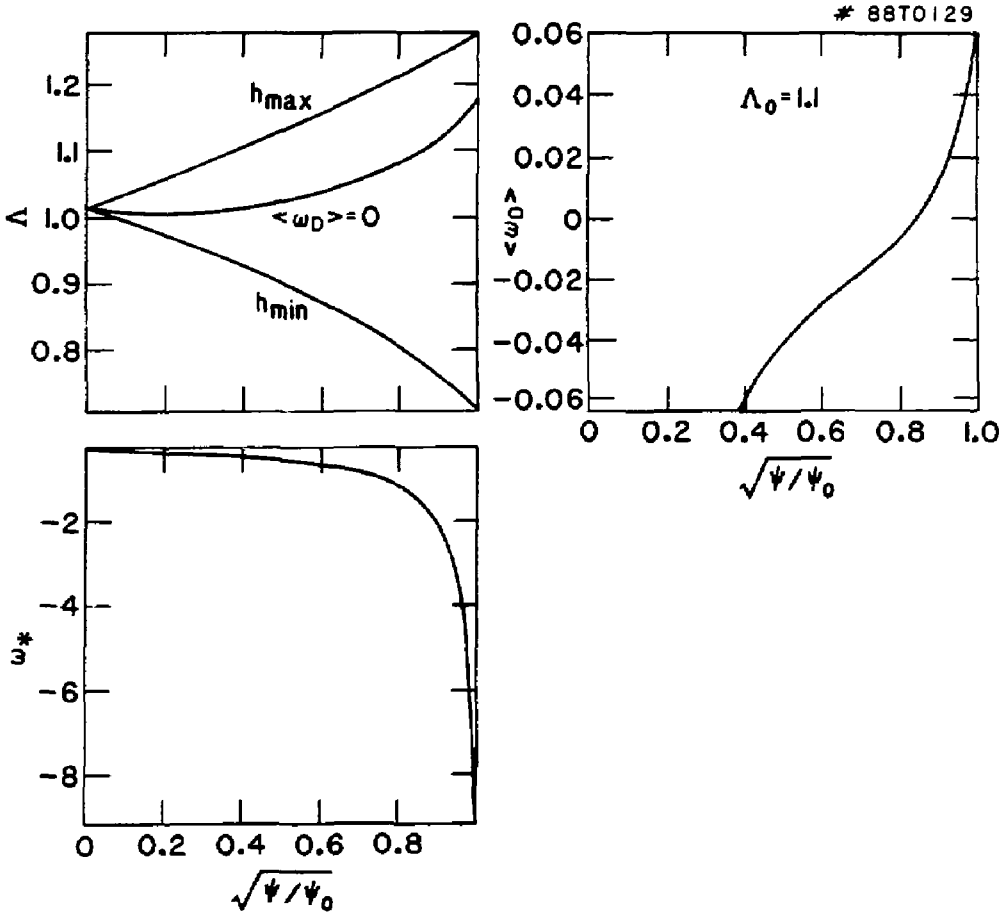
88T0129
1.2
1.1
1.0
0.9
0.8
Λ
h_{max}
$<\omega_D>=0$
h_{min}
0.06
0.04
0.02
0
-0.02
-0.04
-0.06
$<\omega_D>$
$\Lambda_0=1.1$
0
0.2
0.4
0.6
0.8
1.0
$\sqrt{\psi/\psi_0}$
-2
-4
-6
-8
ω^*
0
0.2
0.4
0.6
0.8
$\sqrt{\psi/\psi_0}$

Fig. 6

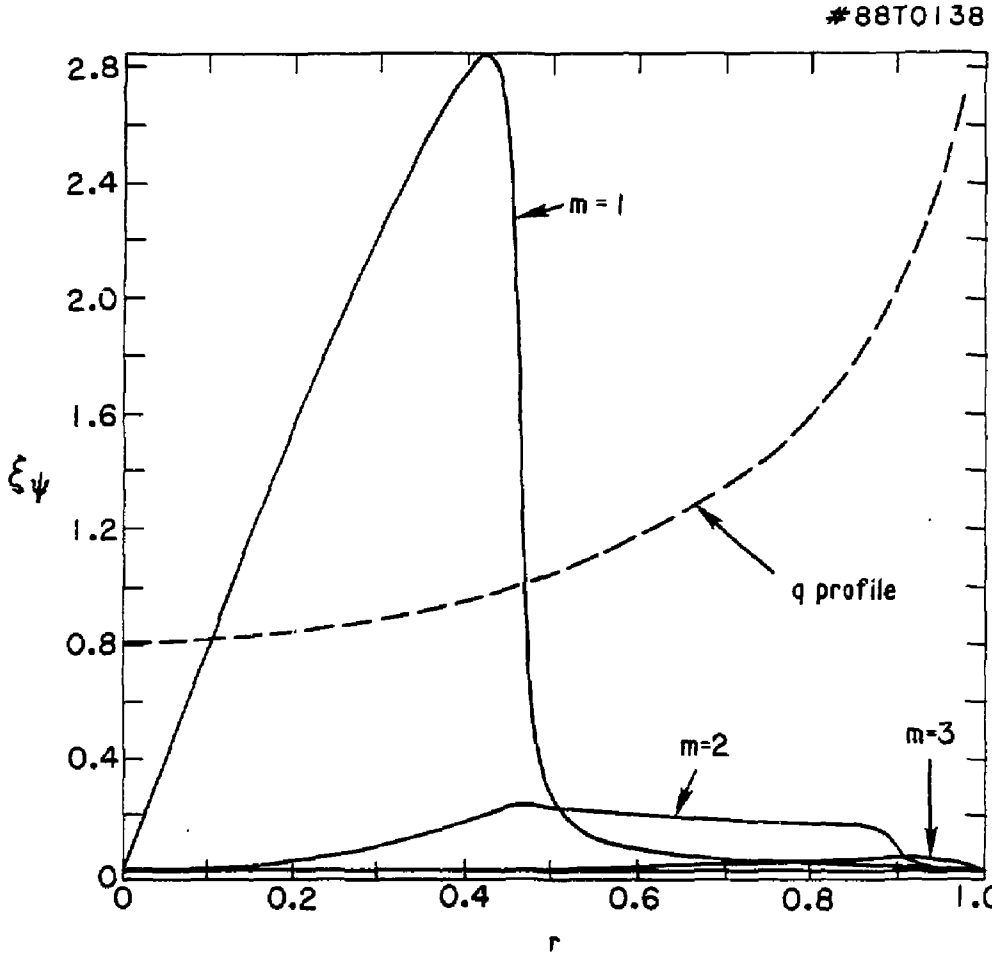
#88T0138
2.8
2.4
2.0
1.6
1.2
0.8
0.4
0
ξ_ψ
m = 1
q profile
m=2
m=3
0
0.2
0.4
0.6
0.8
1.0
r

Fig. 7

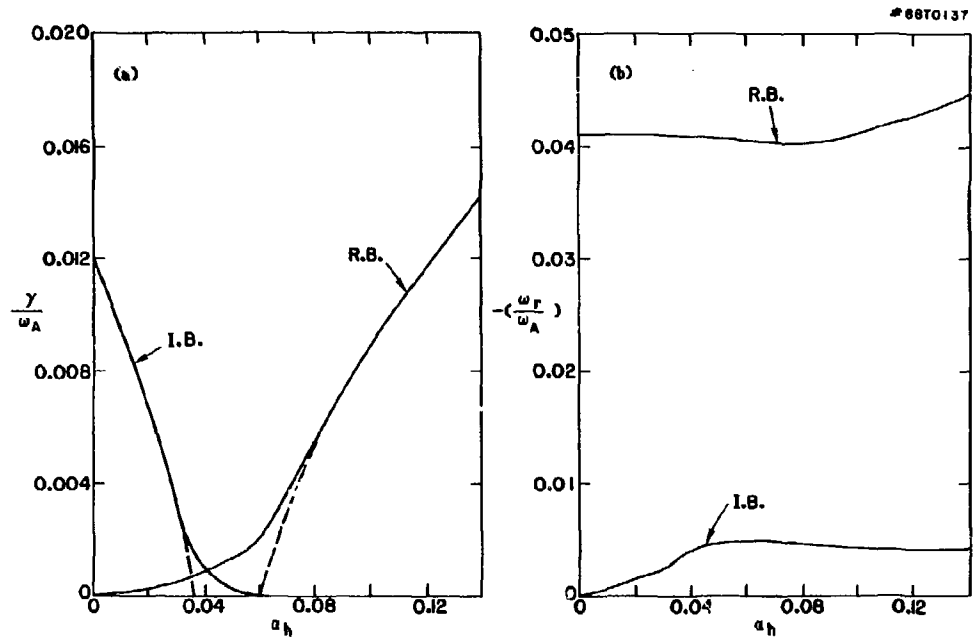
#68T0137
(a)
0.020
0.016
0.012
0.008
0.004
0
$\frac{\gamma}{\omega_A}$
I.B.
R.B.
0
0.04
0.08
0.12
a_h
(b)
0.05
0.04
0.03
0.02
0.01
0
$-(\frac{\omega_r}{\omega_A})$
R.B.
I.B.
0
0.04
0.08
0.12
a_h

Fig. 8

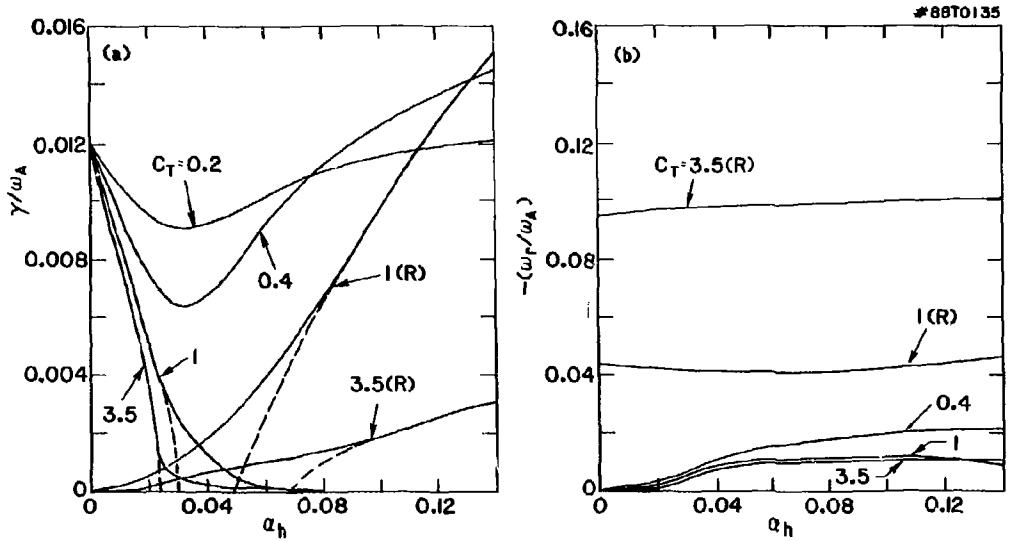
#88T0135
(a)
(b)
γ/ω_A
$-(\omega_r/\omega_A)$
α_h
C_T=0.2
0.4
1(R)
1
3.5
3.5(R)
C_T=3.5(R)
0.016
0.012
0.008
0.004
0
0.16
0.12
0.08
0.04
0.04
0.08
0.12

Fig. 9

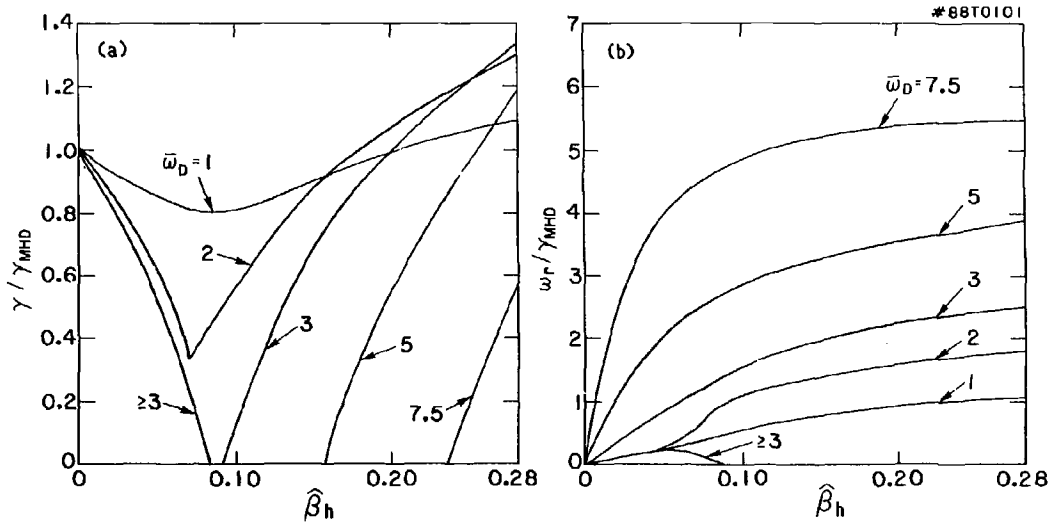
#88T0101
(a)
(b)
γ / γ_{MHD}
ω_r / γ_{MHD}
$\bar{\omega}_D = 1$
2
3
5
7.5
≥3
$\bar{\omega}_D = 7.5$
5
3
2
1
≥3
0
0.10
0.20
0.28
$\hat{\beta}_h$

Fig. 10

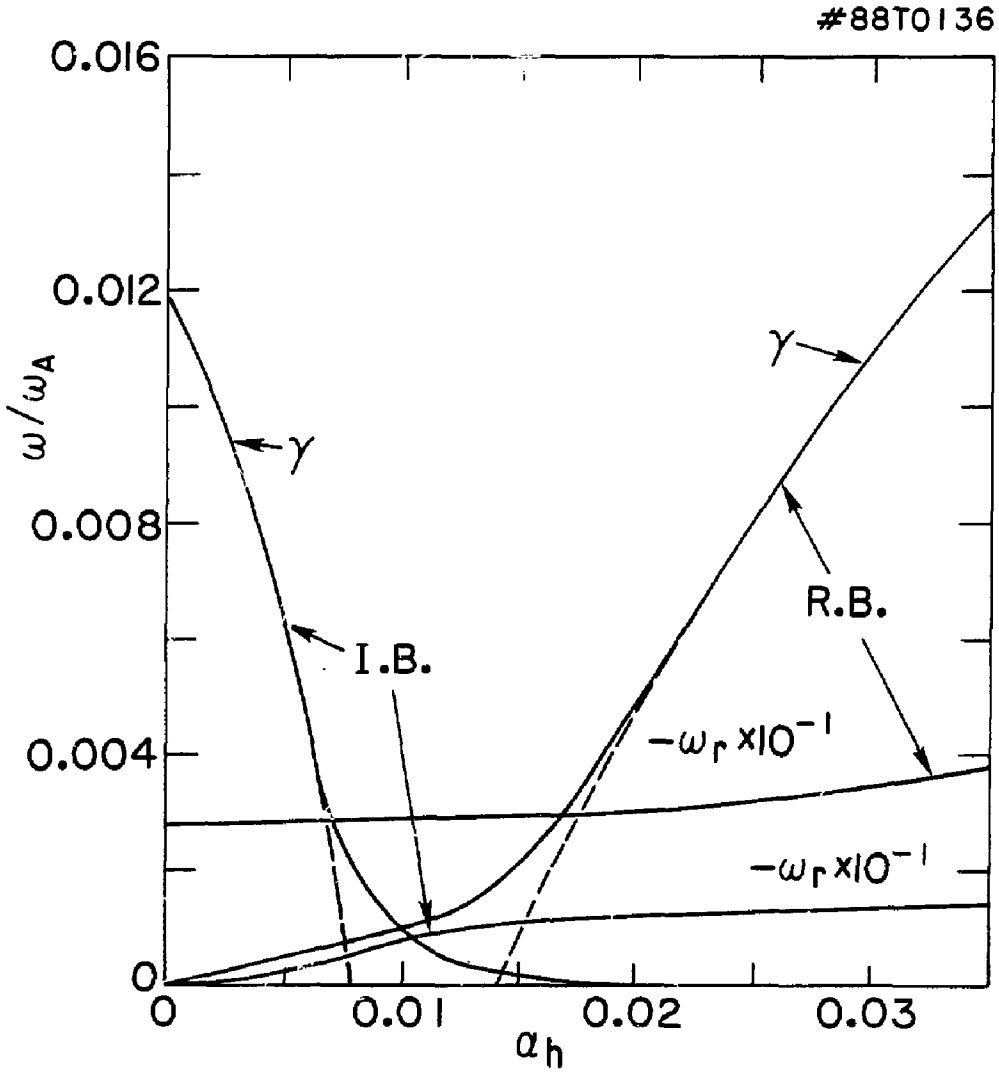
#88T0136
0.016
0.012
0.008
0.004
0
ω/ω_A
γ
γ
I.B.
R.B.
$-\omega_r \times 10^{-1}$
$-\omega_r \times 10^{-1}$
0
0.01
0.02
0.03
α_h

Fig. 11

EXTERNAL DISTRIBUTION IN ADDITION TO UC-20

Dr. Frank J. Paoloni, Univ of Wollongong, AUSTRALIA
Prof. M.H. Brennan, Univ Sydney, AUSTRALIA
Plasma Research Lab., Australian Nat. Univ., AUSTRALIA
Prof. I.R. Jones, Flinders Univ., AUSTRALIA
Prof. F. Cap, Inst Theo Phys, AUSTRIA
Prof. M. Heindler, Institut fur Theoretische Physik, AUSTRIA
M. Goossens, Astronomisch Instituut, BELGIUM
Ecole Royale Militaire, Lab de Phys Plasmas, BELGIUM
Commission-Eurogean, Dg-XII Fusion Prog, BELGIUM
Prof. R. Boucique, Laboratorium voor Natuurkunde, BELGIUM
Dr. P.H. Sakanaka, Instituto Fisica, BRAZIL
Instituto De Pesquisas Espaciasi-INPE, BRAZIL
Documents Office, Atomic Energy of Canada Limited, CANADA
Dr. M.P. Bachynski, MPB Technologies, Inc., CANADA
Dr. H.M. Skarsgard, University of Saskatchewan, CANADA
Dr. H. Barnard, University of British Columbia, CANADA
Prof. J. Teichmann, Univ. of Montreal, CANADA
Prof. S.R. Sreenivasan, University of Calgary, CANADA
Prof. Tudor W. Johnston, INRS-Energie, CANADA
Dr. C.R. James, Univ. of Alberta, CANADA
Dr. Peter Lukac, Komenskeho Univ, CZECHOSLOVAKIA
The Librarian, Culham Laboratory, ENGLAND
The Librarian, Rutherford Appleton Laboratory, ENGLAND
Mrs. S.A. Hutchinson, JET Library, ENGLAND
C. Mouttet, Lab. de Physique des Milieux Ionises, FRANCE
J. Radet, CEN/CADARACHE - Bat 506, FRANCE
Univ. of Ioannina, Library of Physics Dept, GREECE
Dr. Tom Mual, Academy Bibliographic Ser., HONG KONG
Preprint Library, Hungarian Academy of Sciences, HUNGARY
Dr. S. Dasgupta, Saha Inst of Nucl. Phys., INDIA
Dr. P. Kaw, Institute for Plasma Research, INDIA
Dr. Philip Rosenau, Israel Inst. Tech, ISRAEL
Librarian, Int'l Ctr Theo Phys, ITALY
Prof. G. Rostagni, Univ Di Padova, ITALY
Miss Clelia De Palo, Assoc EURATOM-ENEA, ITALY
Biblioteca, Instituto di Fisica del Plasma, ITALY
Dr. H. Yamato, Toshiba Res & Dev, JAPAN
Prof. Y. Kawakami, Atomic Energy Res. Institute, JAPAN
Prof. Kyoji Nishikawa, Univ of Hiroshima, JAPAN
Direc. Dept. Large Tokamak Res. JAERI, JAPAN
Prof. Satoshi Itoh, Kyushu University, JAPAN
Research Info Center, Nagoya University, JAPAN
Prof. S. Tanaka, Kyoto University, JAPAN
Library, Kyoto University, JAPAN
Prof. Nobuyuki Inoue, University of Tokyo, JAPAN
S. Mori, JAERI, JAPAN
Librarian, Korea Advanced Energy Res. Institute, KOREA
Prof. D.I. Choi, Adv. Inst Sci & Tech, KOREA
Prof. B.S. Liley, University of Waikato, NEW ZEALAND
Institute of Plasma Physics, PEOPLE'S REPUBLIC OF CHINA
Librarian, Institute of Phys., PEOPLE'S REPUBLIC OF CHINA
Library, Tsing Hua University, PEOPLE'S REPUBLIC OF CHINA
Z. Li, Southwest Inst. Physics, PEOPLE'S REPUBLIC OF CHINA
Prof. J.A.C. Cabral, Inst Superior Tecnico, PORTUGAL
Dr. Octavian Petrus, AL I CUZA University, ROMANIA
Dr. Johan de Villiers, Fusion Studies, AEC, SO AFRICA
Prof. M.A. Hellberg, University of Natal, SO AFRICA
C.I.E.M.A.T., Fusion Div. Library, SPAIN
Dr. Lennart Stenflo, University of UMEA, SWEDEN
Library, Royal Inst Tech, SWEDEN
Prof. Hans Wilhelmson, Chalmers Univ Tech, SWEDEN
Centre Phys des Plasmas, Ecole Polytech Fed, SWITZERLAND
Bibliotheek, Fom-Inst Voor Plasma-Fysica, THE NETHERLANDS
Dr. D.D. Ryutov, Siberian Acad Sci, USSR
Dr. G.A. Eliseev, Kurchatov Institute, USSR
Dr. V.A. Glukhikh, Inst Electrophysical Apparatus, USSR
Dr. V.T. Tolok, Inst. Phys. Tech. USSR
Dr. L.M. Kovrizhnykh, Institute Gen. Physics, USSR
Nuclear Res. Establishment, Julich Ltd., W. GERMANY
Bibliothek, Inst. Fur Plasmaforschung, W. GERMANY
Dr. K. Schindler, Ruhr Universitat Bochum, W. GERMANY
ASDEX Reading Rm, IPP/Max-Planck-Institut fur Plasmaphysik, W. GERMANY
Librarian, Max-Planck Institut, W. GERMANY
Prof. R.K. Janev, Inst Phys, YUGOSLAVIA